



# Paralog knockout profiling identifies *DUSP4* and *DUSP6* as a digenic dependence in MAPK pathway-driven cancers

Takahiro Ito<sup>1,2,3,4</sup>, Michael J. Young<sup>1</sup>, Ruitong Li<sup>1</sup>, Sidharth Jain<sup>1</sup>, Andreas Wernitznig<sup>1,5</sup>, John M. Krill-Burger<sup>1</sup>, Christopher T. Lemke<sup>1</sup>, Davide Monducci<sup>1</sup>, Diego J. Rodriguez<sup>1</sup>, Liang Chang<sup>1,3</sup>, Sanjukta Dutta<sup>1</sup>, Debjani Pal<sup>1,2,3</sup>, Brenton R. Paoella<sup>1</sup>, Michael V. Rothberg<sup>1</sup>, David E. Root<sup>1</sup>, Cory M. Johannessen<sup>1,6</sup>, Laxmi Parida<sup>7</sup>, Gad Getz<sup>1,3,8</sup>, Francisca Vazquez<sup>1</sup>, John G. Doench<sup>1</sup>, Mahdi Zamanighomi<sup>1</sup> and William R. Sellers<sup>1,2,3</sup> ✉

**Although single-gene perturbation screens have revealed a number of new targets, vulnerabilities specific to frequently altered drivers have not been uncovered. An important question is whether the compensatory relationship between functionally redundant genes masks potential therapeutic targets in single-gene perturbation studies. To identify digenic dependencies, we developed a CRISPR paralog targeting library to investigate the viability effects of disrupting 3,284 genes, 5,065 paralog pairs and 815 paralog families. We identified that dual inactivation of *DUSP4* and *DUSP6* selectively impairs growth in *NRAS* and *BRAF* mutant cells through the hyperactivation of MAPK signaling. Furthermore, cells resistant to MAPK pathway therapeutics become cross-sensitized to *DUSP4* and *DUSP6* perturbations such that the mechanisms of resistance to the inhibitors reinforce this mechanism of vulnerability. Together, multigene perturbation technologies unveil previously unrecognized digenic vulnerabilities that may be leveraged as new therapeutic targets in cancer.**

The development of targeted therapies such as imatinib and gefitinib vastly improved the outcomes of patients with tumors harboring *BCR-ABL* fusion or *EGFR* mutation, respectively. However, we still lack therapies for tumors harboring many known cancer driver aberrations. In efforts to systematically identify new dependencies for particular genetic alterations, over 700 cancer cell lines have been screened by genome-wide CRISPR-Cas9 or RNA interference (RNAi) libraries<sup>1–3</sup>. These studies have revealed new single-gene dependencies such as dependence on the Werner syndrome ATP-dependent helicase in tumors with microsatellite instability and on the protein arginine methyltransferase 5 in cancer cells with deletion of methylthioadenosine phosphorylase<sup>2,4–8</sup>. However, effective new targets relevant to the most common genetically altered drivers (that is, RAS, PTEN, TP53, MYC) have not been uncovered.

Functional redundancies among paralogous genes likely limit the discovery of new dependencies from single-gene perturbation screens<sup>9,10</sup>. However, identifying paralog redundancies is highly complex. Efforts to systematically assess the fitness of multiple genes were initially performed in yeast and *Drosophila* through the generation of digenic and trigenic mutants<sup>11–14</sup>. Genetic interaction screens in human cells are emerging through simultaneous perturbation of two genes in the same cell using multiplex single-guide RNAs (sgRNAs) although these studies were limited to a small number of curated genes in an all-by-all format making combinatorial knockouts of hundreds of distinct paralog families challenging<sup>15–18</sup>.

In this study, we developed a digenic combinatorial perturbation technology to profile dependencies of 815 distinct paralog families. Screening across 11 cancer cell lines identified 686 unique synergistic dependencies missed from the single-gene knockout studies. We identified the dual deletion of *DUSP4* and *DUSP6* (*DUSP4/6*) as digenic synthetic lethal targets in *NRAS* and *BRAF* mutant melanomas through the hyperactivation of ERK signaling. Furthermore, as cells develop resistance to MAPK pathway inhibitors, they are hypersensitized to *DUSP4/6* dual knockouts. This mechanism constitutes a rare example of cross-sensitization between potential therapeutic mechanisms.

## Results

**Functional redundancy of paralogous genes.** Analyses of the single-gene CRISPR screens showed that genes with paralogs are less likely to be essential, potentially due to the compensatory relationships between functional redundant paralogs (Extended Data Fig. 1a). Importantly, we know that the activity of small molecules inhibiting paralogs with conserved binding sites is not recapitulated using short hairpin RNA (shRNA) or sgRNA reagents that target single genes (Fig. 1a). For example, MEK inhibitors have activity in *NRAS* mutant cells whereas individual knockouts of *MAP2K1* (*MEK1*) or *MAP2K2* (*MEK2*) fail to phenocopy pharmacological inhibition or *NRAS* knockout (Extended Data Fig. 1b). Together, these data suggest that single-gene perturbation screens cannot reliably detect new targets composed of functionally redundant paralogous genes.

<sup>1</sup>Broad Institute of Harvard and MIT, Cambridge, MA, USA. <sup>2</sup>Department of Medical Oncology, Dana-Farber Cancer Institute, Boston, MA, USA. <sup>3</sup>Harvard Medical School, Boston, MA, USA. <sup>4</sup>Scorpion Therapeutics, Boston, MA, USA. <sup>5</sup>Boehringer Ingelheim RCV GmbH & Co KG, Vienna, Austria. <sup>6</sup>Oncology, Novartis Institutes for BioMedical Research, Cambridge, MA, USA. <sup>7</sup>IBM Research, T.J. Watson Research Center, Yorktown Heights, NY, USA. <sup>8</sup>Cancer Center and Department of Pathology, Massachusetts General Hospital, Boston, MA, USA. ✉e-mail: [wsellers@broadinstitute.org](mailto:wsellers@broadinstitute.org)

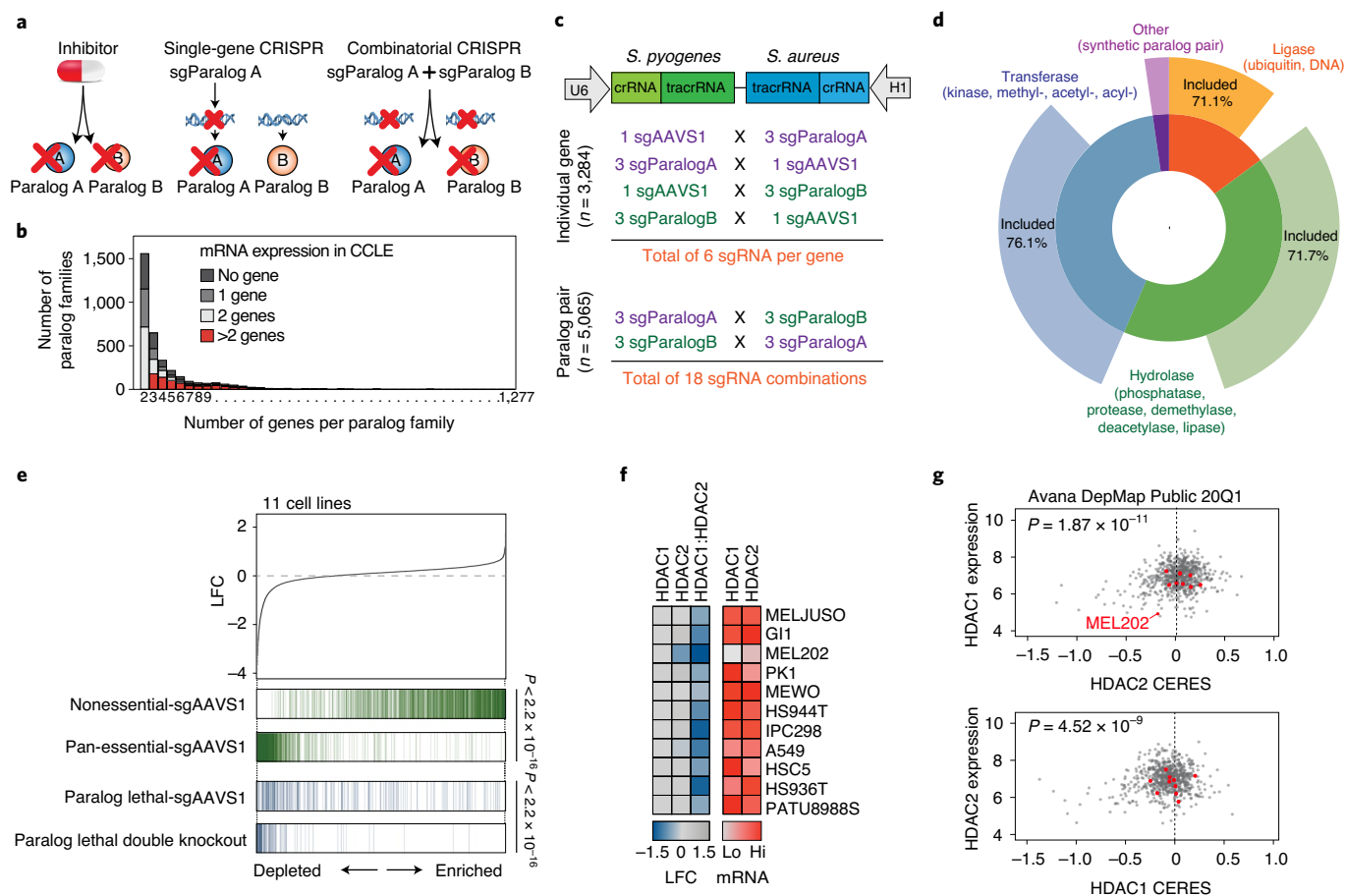


**Fig. 1 | Development and performance of a Digenic Paralog CRISPR library.** **a**, Rationale for perturbation screens targeting paralogous genes. **b**, Number of genes for each paralog family in the human genome. Each paralog family is color-coded by the number of expressed genes across CCLE RNA-seq samples (expressed gene defined as  $\log_2(\text{TPM} + 1) > 2$  in at least 50% of 1,270 cell lines). **c**, Schematic of the library design. **d**, Pie chart depicting the percentage of genes included in the Digenic Paralog CRISPR library for each of the protein classes. **e**, Rank-ordered LFC of the Digenic Paralog screens across 11 cell lines (top). Nonessential ( $n = 119$ ) or pan-essential ( $n = 96$ ) genes paired with sgAAVS1 are shown as green lines. Synthetic lethal paralog genes paired with sgAAVS1 ( $n = 22$ ) and dual knockouts targeting the synthetic lethal paralog pairs ( $n = 11$ ) are shown as blue lines (bottom).  $P$  values were calculated according to a one-tailed  $t$ -test. **f**, Heatmap of inferred LFC for sgRNAs targeting *HDAC1*, *HDAC2* or both (left) from the Digenic Paralog CRISPR screen and CCLF RNA-seq data for the expression of *HDAC1* and *HDAC2* (right). **g**, Relationship between *HDAC1* and *HDAC2* expression and DepMap CRISPR-Cas9 single-gene knockout scores ( $n = 722$  cell lines). Cell lines screened by the Digenic Paralog CRISPR library are annotated in red.  $P$  values were calculated based on Pearson correlation.

**Digenic CRISPR-Cas9 screens.** Since paralog families are composed of varying numbers of genes, we first examined the number of paralogous gene perturbations that might be required to test a large portion of functional redundancies. Paralog families consisting of only two genes were the most prevalent across the human genome (Fig. 1b). Additionally, among paralog families containing more than two genes, in many cases only two or fewer genes are expressed, suggesting that pairwise perturbation should capture a significant fraction of paralog redundancies.

We adapted an orthologous Cas9 enzyme system from *Staphylococcus aureus* and *Streptococcus pyogenes* (Big Papi; paired *S. aureus* and *S. pyogenes* for interactions)<sup>17</sup> to develop the Digenic Paralog CRISPR library. In contrast to previous combinatorial CRISPR libraries (one all-by-all gene matrix), our unique cloning design enabled simultaneous perturbation of 3,284 individual genes (6 sgRNAs per gene coupled with an AAVS1 sgRNA cutting control) and 5,065 paralog pairs (18 sgRNA combination pairs) for a total library size of 110,874 constructs targeting 815 distinct paralog families ranging up to 27 genes per family (Fig. 1c). Importantly,

our two-step cloning strategy, first cloning the pair of CRISPR RNAs (crRNA) followed by the introduction of the trans-activating crRNA (tracrRNA) sequences, enabled the direct synthesis of specific sgRNA pairs (Extended Data Fig. 1c).

Since a genome-wide dual paralog CRISPR library would result in a vast library size, the Digenic Paralog CRISPR library focused primarily on enzymatic paralogous genes belonging to transferase (for example, kinases, methyltransferases; 1,344 genes), hydrolase (for example, phosphatases, demethylases; 1,174 genes) and ligase (for example, E3-ubiquitin ligases, DNA ligases; 595 genes) protein classes (Fig. 1d). Genes without paralogs were excluded from the library because the single-gene knockout viability phenotypes have been previously characterized<sup>2</sup>. After library cloning, the cumulative distribution of sgRNAs for the Digenic Paralog and Big Papi libraries using the orthologous Cas9 system was robust in comparison to published combinatorial libraries (Extended Data Fig. 1d)<sup>15,17,19,20</sup>. The utilization of orthologous tracrRNA scaffolds from *S. pyogenes* and *S. aureus* alleviated recombination/uncoupling events with average rates of 1.00% from the plasmid

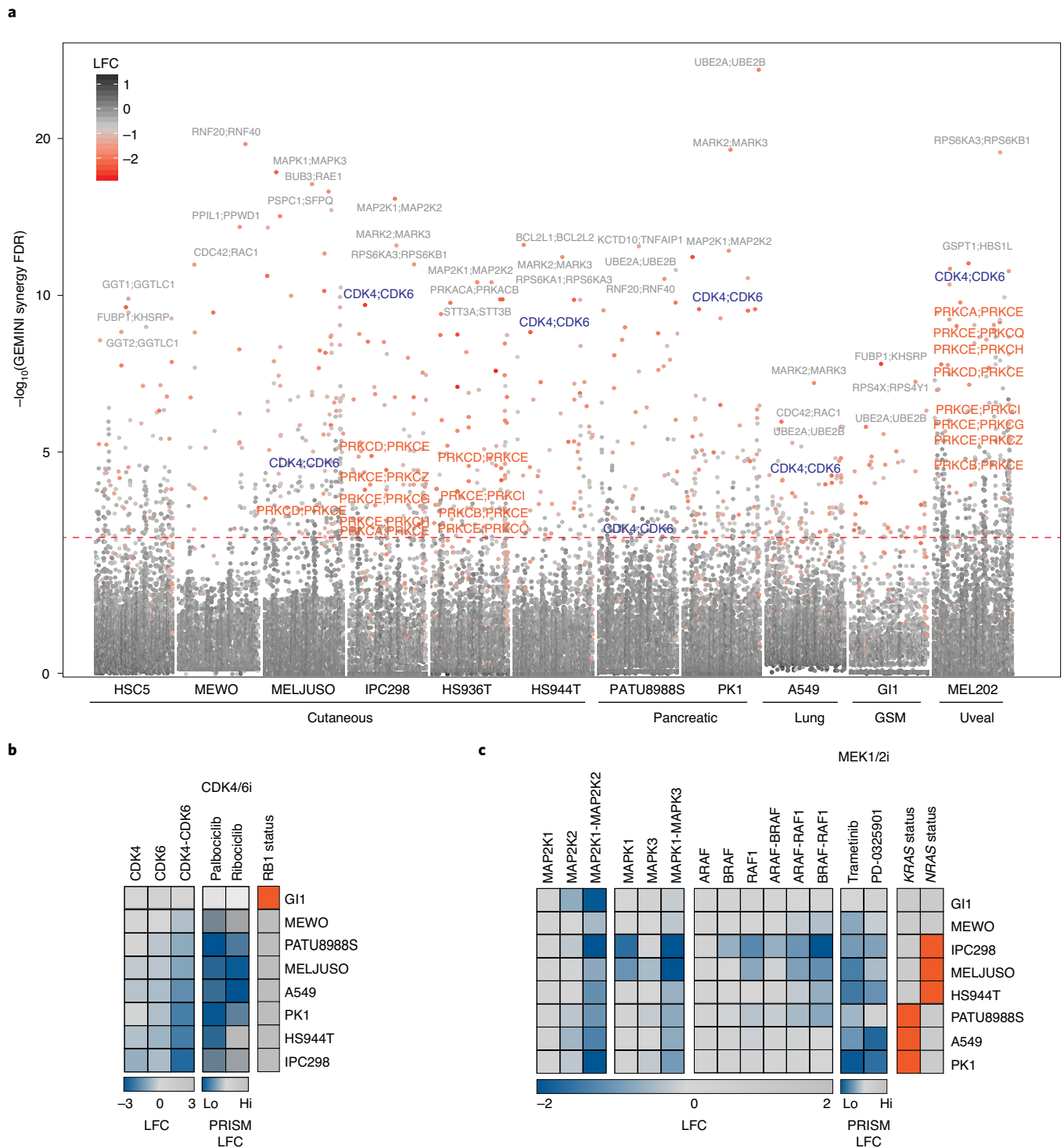


**Fig. 2 | Synergistic paralog dependencies and small-molecule inhibitor profiles.** **a**, Manhattan plot of FDRs corresponding to GEMINI synergy scores and color-coded by the LFC of dependencies for paralog pair knockouts. The top three synergistic pairs are annotated in gray. Significant paralog pairs with PRKCE and CDK4/6 pairs are annotated in orange and blue, respectively. GSM, gliosarcoma. **b**, Heatmap of inferred LFC for sgRNAs targeting *CDK4*, *CDK6* or both (left) and LFC for palbociclib and ribociclib from the drug sensitivity screen (PRISM Repurposing Primary Screen, 20Q1 public dataset; middle). The *RB1* damaging mutation is annotated in orange (right). **c**, Heatmap of inferred LFC for sgRNAs targeting the indicated gene or paralog pairs (left) and LFC for trametinib and PD-0325901 from the drug sensitivity screen (middle). *KRAS* and *NRAS* Catalogue Of Somatic Mutations In Cancer (COSMIC v.94) hotspot mutations are annotated in orange (right).

DNA (pDNA) and 8.37% from genomic DNA (gDNA) (Extended Data Fig. 1e).

We screened this library in a panel of 11 cancer cell lines stably expressing *S. pyogenes* Cas9 in biological triplicates. As an initial

quality check, we evaluated the correlation of the biological triplicates for each cell line that clustered together (Extended Data Fig. 2a). To assess the library efficiency of single-gene knockouts, we examined gene dependence based on single-gene CRISPR knockout

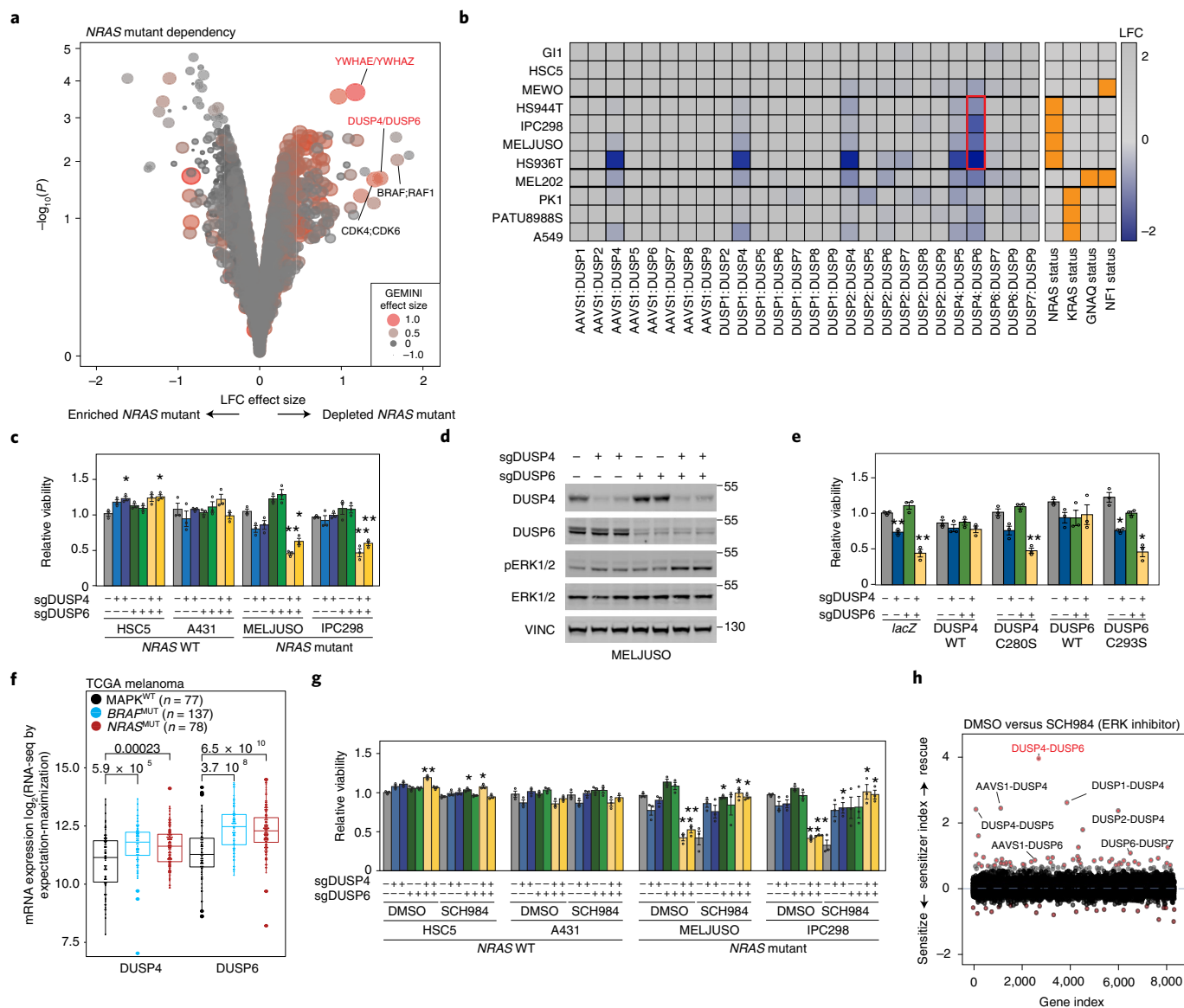


**Fig. 3 | DUSP4/6 are synergistic dependencies in NRAS mutant cells through the hyperactivation of ERK.** **a**, Paralog pairs showing differential dependence between NRAS mutant (MELJUSO, IPC298, HS944T and HS936T) and NRAS WT (GI1, HSC5) cells. The mean difference of LFC and P values (empirical Bayes moderated *t*-test) are plotted. Each point is annotated by color and size of the mean difference of the GEMINI synergy score. **b**, Heatmap of LFC between all *DUSP* gene and paralog pairs (left). Cell lines harboring COSMIC hotspot mutations to *NRAS*, *KRAS*, *GNAQ* or damaging mutations to *NF1* are annotated in orange (right). **c**, Relative viability of cells infected with a dual promoter lentiviral vector expressing two *S. pyogenes* sgRNAs. Two different sgRNA pairs were used against *DUSP4* or *DUSP6*; sgRNAs targeting AAVS1 and CHR2 sites were used as controls. **d**, Immunoblot of indicated proteins in MELJUSO 2 d after sgRNA transduction and antibiotic selection. **e**, Relative viability for MELJUSO cells ectopically expressing sgRNA-resistant WT or phosphatase-dead *DUSP4* (C280S) or *DUSP6* (C293S) cDNA infected with sgRNAs targeting *DUSP4*, *DUSP6* or both. **f**, Box and whisker plots for *DUSP4/6* expression (TCGA) in melanoma tumors harboring the *BRAF* or *NRAS* mutation compared to melanoma tumors with no known MAPK signaling pathway mutations (MAPK<sup>WT</sup>). Two-sided Mann-Whitney *U*-test *P* values are shown. The centerline, lower hinge and upper hinge correspond to the 50th, 25th and 75th percentiles, respectively. The upper and lower whiskers extend from the upper and lower hinges to the largest and smallest values no further than 1.5x the interquartile range. **g**, Relative viability in cells infected with the indicated sgRNAs in the presence of DMSO or SCH772984 (78 nM). **h**, Cas9-stable MELJUSO cells were infected with the Digenic Paralog CRISPR library and divided and grown in continuous DMSO- (*n*=1) or SCH772984-containing (78 nM; *n*=2) media. Plot showing the sensitizer index (LFC SCH772984/LFC DMSO) plotted to the gene index (randomized gene order). **c,e,g**, Data are from three independent experiments. Data are shown as the mean ± s.e.m. \**P* < 0.01, \*\**P* < 0.001, unpaired two-sided *t*-test.

from our screen (single-gene sgRNAs paired with sgAAVS1) and observed strong dependencies on previously identified pan-essential genes but not on previously identified nonessential genes (Fig. 1e)<sup>21</sup>. These dependency measurements were highly correlated to the single-gene knockout data obtained with the Avana library (Pearson

coefficient = 0.83) as well as between the *S. pyogenes* and *S. aureus* sgRNAs (Pearson coefficient = 0.62; Extended Data Fig. 2b,c).

To evaluate the efficiency of the dual knockout, we focused on the positive control examples of known lethal paralog pairs (Methods). These paralog pairs were identified from the single-gene knockout

studies where lethal interactions arise from the genetic inactivation, through mutation, deletion or transcriptional downregulation of one member of a pair of paralogous genes leading to dependence on the remaining paralog. These included *ARID1B* as a vulnerability in *ARID1A*-deficient cells<sup>22</sup>. We hypothesized that dual knockout of these synthetic paralog lethal genes would likely be essential in most cell lines. Indeed, the double knockouts were lethal and exhibited significantly stronger dependencies compared to their corresponding single-gene knockouts (Fig. 1e). For example, the double knockout of *HDAC1* and *HDAC2* was synergistic and lethal across all cell lines except MEL202, which exhibited single-gene dependency on *HDAC2*, probably due to low *HDAC1* expression (Fig. 1f). This agrees with the DepMap data, where cell lines having low *HDAC1* expression are dependent on the single-gene knockout of *HDAC2* and vice versa (Fig. 1g). Collectively, these observations demonstrate the efficacy of the Digenic Paralog CRISPR library in detecting known dependencies of both the essential single-gene and dual paralog pairs.

**The landscape of synergistic paralog pairs.** To systematically identify genetic interactions and synergy, we developed and utilized a variational Bayesian approach (GEMINI; Fig. 2a)<sup>23</sup>. We found 686 unique synergistic paralog pairs (13.5% of paralog pairs in the library) with a false discovery rate (FDR) below 5% across the 11 cell lines with varying degrees (Extended Data Fig. 3a). Additionally, 22% of the 3,284 single genes showed synergistic effects with at least one member of the paralog family (Extended Data Fig. 3b). The synergistic pairs were distributed equally among the three major protein classes and paralog family size (Extended Data Fig. 3c). Surprisingly, only 1.73% of the paralog pairs were synergistically essential in more than seven cell lines (Extended Data Fig. 3d). We observed that basal expression of both of the genes increased the probability of exhibiting synergistic genetic interactions (Extended Data Fig. 3e).

To identify synergistic paralog pairs that recapitulate the potential profile of small-molecule inhibitors, we screened a uveal melanoma (UM) cell line (MEL202) harboring an activating mutation in *GNAQ* (Q209L), a common mutation seen in patients with UM. *GNAQ* signaling activates the protein kinase C (*PRKC*) family that consists of at least nine paralogous genes. Previous studies showed that UM cells have increased sensitivity to *PRKC* inhibitors<sup>24</sup>. We observed that knockout of *PRKCE* together with multiple other members of the *PRKC* gene family synergistically suppresses fitness in MEL202 (Fig. 2a and Extended Data Fig. 3f,g).

Additionally, although single-gene knockouts of either *CDK4* or *CDK6* are not a marked dependence in cell lines screened with the Digenic Paralog library, dual CRISPR knockouts of *CDK4* and *CDK6* exhibited a similar sensitivity profile to pharmacological inhibitors of *CDK4/6* (palbociclib and ribociclib). The GI1 gliosarcoma cell line was completely unresponsive to both genetic and pharmacological inhibition of *CDK4* and *CDK6* since it harbors damaging mutations to *RB1* (R552\*), a known substrate of *CDK4/6* whose loss confers resistance to *CDK4/6* inhibitors (Fig. 2b)<sup>25</sup>.

We hypothesized that cell lines harboring activating mutations in *NRAS* or *KRAS* would exhibit selective sensitivity to the dual knockout of *MAP2K1-MAP2K2*, *MAPK1-MAPK3* (*ERK2-ERK1*) and *BRAF-RAF1*. Dual CRISPR knockout of *MAPK1-MAPK3* or dual knockout of *BRAF-RAF1* impaired proliferation of a subset of *NRAS* and *KRAS* mutant cell lines, while dual perturbation of *MAP2K1-MAP2K2* impaired growth in all cell lines (Fig. 2c). These data suggest that the dual paralog knockouts can recapitulate the profiles of pharmacological inhibitors as seen for *PRKC* and *CDK4/6* inhibitors. On the other hand, dual *MAP2K1-MAP2K2* knockout failed to fully phenocopy the pharmacological inhibitors that might reflect qualitative or quantitative differences in signaling caused by fully eliminating these kinases compared to occupying their catalytic sites.

**DUSP4/6 as targets in *NRAS* mutant melanoma.** To examine whether the Digenic Paralog screens could identify context-specific digenic dependencies, we evaluated selective dependencies (log<sub>2</sub> fold change (LFC)) and synergies (GEMINI) between different indications (Extended Data Fig. 4a,b). Surprisingly, comparison in cells with *NRAS* mutation (MELJUSO, IPC298, HS944T, HS936T; all cutaneous melanoma cell lines) to models with MAPK pathway wild-type (WT) status (GI1, HSC5) revealed several paralog pairs that selectively affected the growth in *NRAS* mutant cells including *YWHAE* and *YWHAZ* ( $P=2.1 \times 10^{-4}$ ), the specific 14-3-3 dimeric proteins that bind to *RAF1* and *BRAF* to maintain an auto-inhibited state and participate in the activation of the MAPK pathway by driving the formation of *RAF* dimers on *RAS* signaling (Fig. 3a)<sup>26</sup>.

A paralog pair that exhibited even stronger synergistic vulnerability on dual knockout was dual specificity phosphatases 4 and 6 (*DUSP4/6*), phosphatases that play roles in the negative feedback regulation of MAPK signaling ( $P=2.15 \times 10^{-2}$ ) (Fig. 3a,b and Extended Data Fig. 4c). *DUSP6* dephosphorylates *ERK* while *DUSP4* dephosphorylates *ERK*, *p38* and *JNK*<sup>27</sup>.

We next examined and validated the mechanistic link between *DUSP4/6* knockout and *NRAS* mutation. Knockout of *DUSP4* or *DUSP6* individually with two independent sgRNAs had no growth effects in both MAPK pathway WT and *NRAS* mutant cell lines. By contrast, the dual knockout of *DUSP4/6* markedly inhibited cell growth and increased *ERK* phosphorylation in *NRAS* mutant cell lines but had no effects in the MAPK pathway WT cell lines (Fig. 3c,d and Extended Data Fig. 4d). Ectopic expression of an sgRNA-resistant complementary DNA (cDNA) of *DUSP4* or *DUSP6* fully rescued the proliferation effect and attenuated the increased phosphorylation of *ERK* in the *NRAS* mutant cell line MELJUSO on double knockout of *DUSP4/6*, suggesting that growth inhibition requires the dual knockout of both *DUSP4/6* (Fig. 3e and Extended Data Fig. 4e). Moreover, ectopic expression of sgRNA-resistant, catalytically inactive *DUSP4* (C280S) or *DUSP6* (C293S) failed to rescue growth inhibition and maintained increased *ERK* phosphorylation on dual knockout of *DUSP4/6* (Fig. 3e and Extended Data Fig. 4e). Together, these data suggest that genetic suppression of *DUSP4/6* induces growth arrest in *NRAS* mutant cutaneous melanoma cells through their phosphatase activity.

**Elevated *DUSP4/6* in MAPK mutant cells.** *DUSP4/6* are negative feedback regulators and transcriptional targets downstream of the MAPK pathway<sup>28</sup>. Indeed, melanoma tumors from The Cancer Genome Atlas (TCGA) harboring oncogenic *NRAS* or *BRAF* mutation show increased expression of *DUSP4/6* compared to MAPK pathway WT tumors (Fig. 3f). Additionally, ectopic expression of activated *NRAS* cDNA (Q61R) in a MAPK pathway WT skin squamous cell line induced increased levels of both *DUSP4* and *DUSP6* (Extended Data Fig. 4f). These data suggest that *NRAS* mutant tumors exhibit increased levels of *DUSP4/6* and that the inhibition of these phosphatases might represent a synthetic lethal dependency in *NRAS* mutant cells while having less adverse toxicities in healthy human cells; however, this is to be determined.

**Loss of *DUSP4/6* hyperactivates *ERK*.** We next hypothesized that dual inhibition of *DUSP4/6* might result in the hyperactivation of *ERK*, a shared substrate of *DUSP4/6*, creating vulnerabilities in cells with preexisting oncogenic mutations in the MAPK pathway<sup>29-33</sup>. To test this hypothesis, we examined cell proliferation on double knockout of *DUSP4/6* in the presence or absence of the *ERK* (SCH772984) or *MEK* (trametinib) inhibitor and showed that the growth arrest induced by dual knockout of *DUSP4/6* can be rescued by *ERK* and *MEK* inhibition (Fig. 3g and Extended Data Fig. 4g). Moreover, we sought to determine which paralog dependencies were most dependent on *ERK* activation. To this end, we performed the paralog CRISPR screen in a *NRAS* mutant cell line in the

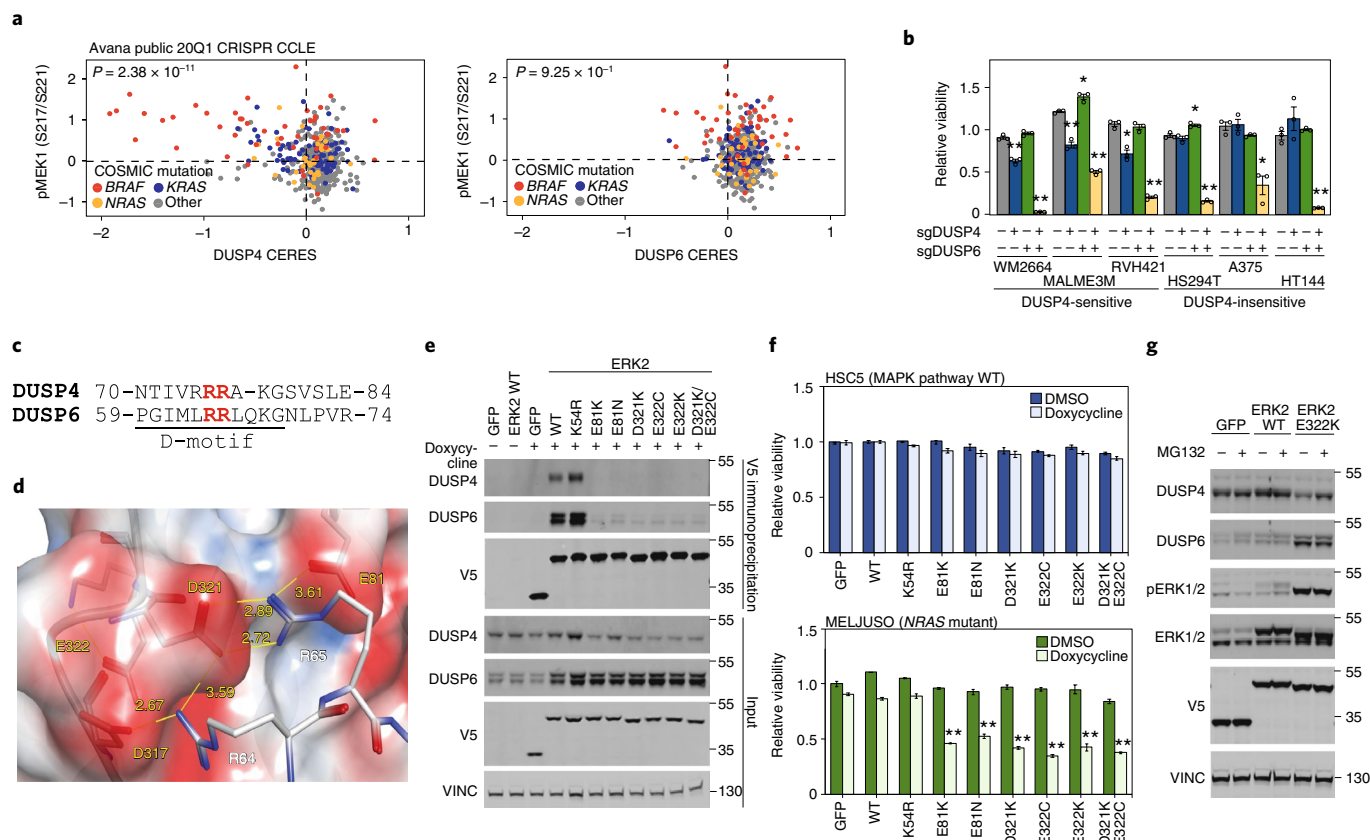


**Fig. 4 | ERK2 DRS is required for DUSP4/6 binding.** **a**, Scatter plot comparing DUSP4 (left) or DUSP6 (right) DepMap CERES scores to phospho-MEK1 (pMEK1) (S217/S221) levels measured by reverse-phase protein array annotated by COSMIC hotspot mutations to *BRAF*, *NRAS* and *KRAS*. *P* values were calculated based on linear regression analysis. **b**, Relative viability with sgRNAs targeting *DUSP4*, *DUSP6* or both in *BRAF* mutant melanoma cells. **c,d**, Sequence alignments of the D-motif sequences for DUSP4/6 (**c**) and the D-motif of DUSP6 in complex with ERK2 (**d**) (based on Protein Data Bank ID 2FY5 with energy minimized to diminish the potential effect of crystallization contact artifacts). The key residues of ERK2 and DUSP6 are colored yellow and white, respectively. The semitransparent surface of ERK2 is colored by electrostatic potential (red, negative; blue, positive). Potential hydrogen bonds are indicated by the yellow lines. Distances are indicated in angstroms. **e**, Coimmunoprecipitation of WT or mutant ERK2 with endogenous DUSP4/6 in MELJUSO. Cells were treated with or without 2  $\mu$ M of doxycycline for 48 h. **f**, Relative viability in cells ectopically expressing the ERK2 variant in MAPK pathway WT HSC5 or *NRAS* mutant MELJUSO. **g**, Immunoblot of indicated proteins in cells ectopically expressing GFP, WT or E322K ERK2 treated with or without MG132. **b,f**, Data are from three independent experiments. Data are shown as the mean  $\pm$  s.e.m. \**P*  $\leq$  0.01, \*\**P*  $\leq$  0.001 by unpaired two-sided *t*-test.

presence or absence of a half maximal inhibitory concentration dose of SCH722984 (78 nM). Comparison between the SCH722984 and dimethylsulfoxide (DMSO) screens showed that while the combinatorial knockout of *DUSP4/6* induced growth arrest in the DMSO arm, growth perturbation on dual knockout of *DUSP4/6* was most significantly rescued by ERK inhibition (Fig. 3h and Extended Data Fig. 4h). These data suggest that *DUSP4/6* double knockout induces growth arrest in *NRAS* mutant cells through the hyperactivation of the MAPK pathway.

**DUSP4/6 is a dependency in *BRAF* mutant melanoma cells.** The results above led us to examine the dependency on DUSP family phosphatases in the setting of additional MAPK pathway mutant cells. Analyses of the DepMap single-gene CRISPR knockout screens showed that *DUSP4* single-gene knockout was one of the four dependencies most highly correlated with *BRAF* CRISPR knockout and mutation (Extended Data Fig. 5a,b). Additionally, in the small subset of *BRAF* mutant cell lines that are dependent on *DUSP4* (approximately 20%), this dependence was correlated with high phosphorylation of MEK1 (Fig. 4a) and high messenger RNA expression or protein levels of DUSP4/6 (Extended Data Fig. 5c,d). Although DUSP6 has been reported as a potential target

in *KRAS/EGFR* mutant lung adenocarcinoma, in unbiased perturbation screens and validations we did not observe growth disadvantages on perturbation of *DUSP6* alone and only observed dual dependencies to *DUSP4/6* knockouts in one cell line (Fig. 4a and Extended Data Fig. 5e)<sup>34</sup>.

These data raised the possibility that a broader array of *BRAF* mutant melanoma cell lines might be dependent on the combined *DUSP4/6* knockout. Hence, we asked whether the knockouts of *DUSP4/6* also synergized in *BRAF* mutant cell models. Consistent with the DepMap data (Fig. 4a), single knockout of *DUSP4* alone caused growth arrest in several *BRAF* mutant cell lines (WM2664, MALME3M and RVH421), whereas other cell lines were not responsive (HS294T, A375 and HT144) (Fig. 4b). Interestingly, the dual knockout of *DUSP4/6* inhibited growth to a greater extent than the single *DUSP4* knockout in the *DUSP4*-sensitive cell lines and converted *DUSP4*-insensitive *BRAF* mutant cell lines to sensitive (Fig. 4b). These data suggest that dual perturbations of *DUSP4/6* are dependencies in both *NRAS* and *BRAF* mutant melanoma encompassing approximately 70% of all melanomas.

**ERK2 D-recruitment site as the critical DUSP4/6 interaction site.** Due to the historical challenges in developing selective

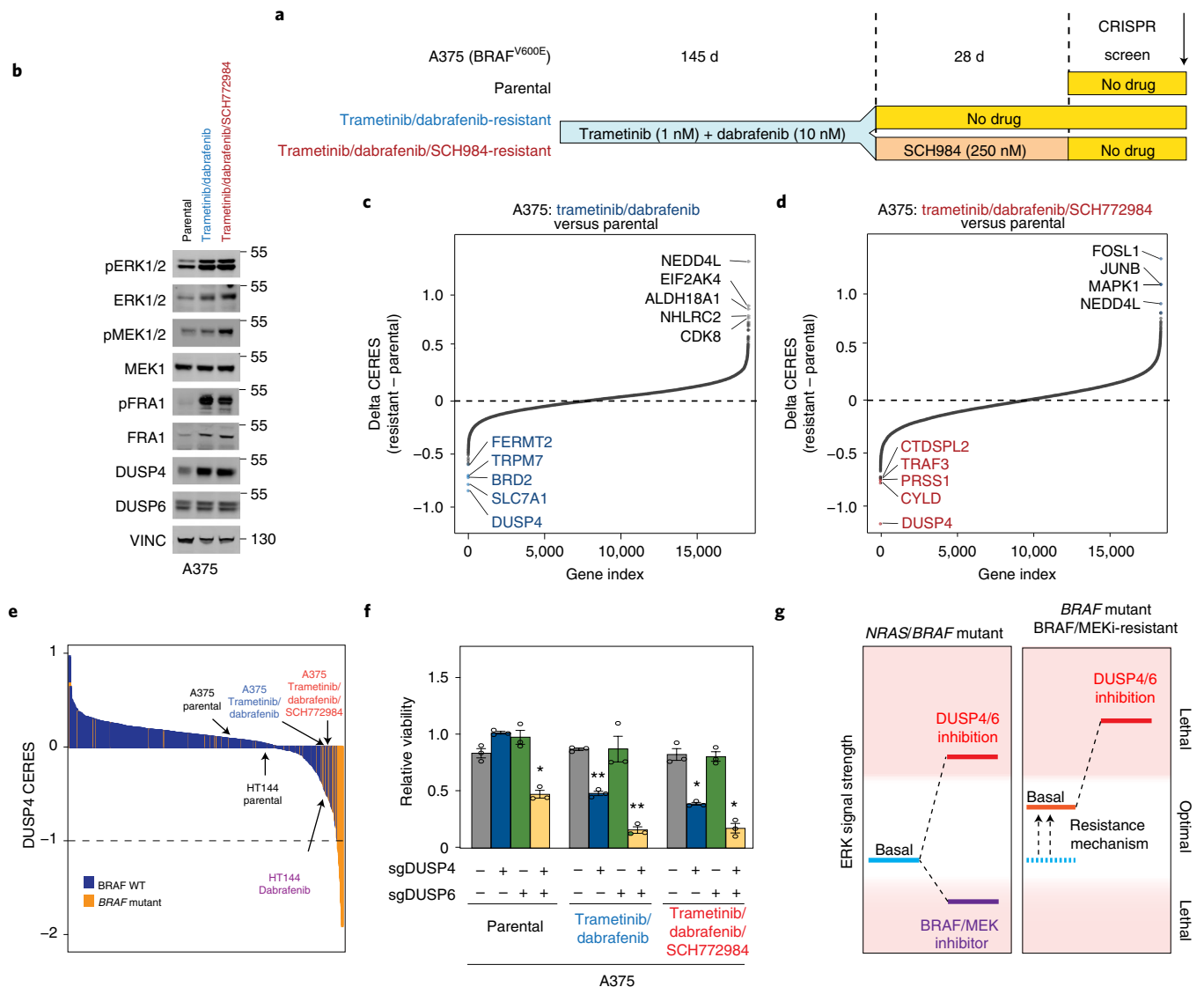


**Fig. 5 | BRAF mutant melanomas resistant to MAPKi are hypersensitized to dual DUSP4/6 knockout.** **a**, Schematic of A375 cell lines resistant to trametinib and dabrafenib or trametinib, dabrafenib and SCH772985. **b**, Immunoblot analysis against the indicated antibodies from total cell lysates for parental and MAPKi-resistant A375. **c,d**, Rank-ordered depiction of the difference in CERES score between A375 cells resistant to trametinib/dabrafenib (**c**) or trametinib/dabrafenib/SCH772984 (**d**) to parental A375 from the genome-wide single-gene CRISPR screen. Delta CERES was calculated by CERES A375<sup>Resistant</sup> – CERES A375<sup>Parental</sup>. **e**, CERES waterfall plot for sgRNAs targeting *DUSP4*, colored by COSMIC *BRAF* mutation (orange). **f**, Relative viability with sgRNAs targeting *DUSP4*, *DUSP6* or both in parental or MAPKi-resistant A375. **g**, Model of *DUSP4/6* dependence in MAPK mutant cells and cross-sensitization in MAPKi-resistant cells. **f**, Data are from three independent experiments. Data are shown as the mean  $\pm$  s.e.m. \* $P \leq 0.01$ , \*\* $P \leq 0.001$  by unpaired two-sided *t*-test.

phosphatase inhibitors, we sought an alternative means of inducing *DUSP4/6*-dependent hyperactivation of ERK. Signal modulation of MAP kinases is frequently achieved by proteins that selectively bind through the MAPK D-recruitment site (DRS), a highly adaptable binding pocket that can bind a wide variety of complementary sequences. *DUSP4/6* carry complementary D-motifs at their N termini. Together, these observations suggest that targeting the ERK DRS may present an elegant and effective strategy to recapitulate the digenic dependence of *DUSP4/6* knockout in *NRAS* mutant cell lines.

Saturation mutagenesis studies of ERK2 have shown that gain-of-function mutations at the DRS increase the phosphorylation of ERK2 in a *DUSP6*-dependent manner<sup>31</sup>. Additionally, based on the crystal structure of ERK2 in complex with the *DUSP6* D-motif<sup>35</sup>, we hypothesized that the electrostatic interactions formed

between the acidic residues of the ERK2 DRS (E81, D321 and E322) with two highly conserved, positively charged arginine residues at the N terminus of the *DUSP4/6* D-motif are critical for the pairing (Fig. 4c,d).

To first test whether the ERK2 DRS is required for its interaction with *DUSP4/6*, we ectopically expressed WT, kinase-dead (K54R) or DRS mutant (E81K, E81N, D321K, E322C, E322K and D321K/E322C) ERK2 in MELJUSO cells and evaluated the ability of these proteins to interact with endogenous *DUSP4/6*. In coimmunoprecipitation experiments, the ERK2 DRS mutant constructs failed to bind to endogenous *DUSP4/6*, while the non-DRS-mutated ERK2 constructs exhibited robust interactions (Fig. 4e), suggesting that the DRS of ERK2 is required for interacting with both *DUSP4/6*. To test whether the observed disruption of the ERK2-*DUSP4/6* interaction is sufficient to recapitulate the growth arrest phenotype

of the DUSP4/6 digenic dependency, these same ERK2 constructs were ectopically expressed in both the *NRAS* mutant MELJUSO cell line and the MAPK pathway WT HSC5 cell line. Convincingly, the DRS mutant but not the WT *ERK2* induced growth arrest in the MELJUSO but not in the HSC5 cells as seen previously in *BRAF* mutant melanoma (Fig. 4f)<sup>31</sup>. Additionally, we observed decreased protein levels of DUSP4 in cells expressing the *ERK2* DRS mutant, which is consistent with previous studies that showed destabilization of DUSP4 unbound to substrate<sup>36</sup>. Interestingly, the decrease of DUSP4 protein levels in cells ectopically expressing the DRS mutant (E322K) *ERK2* was partially rescued on treatment with a proteasome inhibitor, MG132 (Fig. 4g). Altogether, the ERK2 DRS is a critical domain for DUSP4/6 binding; loss of ERK2-DUSP4 binding results in the degradation of DUSP4 and recapitulates the digenic dependency of DUSP4/6 knockout in *NRAS* mutant cell lines.

### Cross-sensitization of MAPK inhibitor-resistant cells to DUSP4/6.

A challenge to the treatment of patients with *BRAF* mutant cancers is the development of resistance to BRAF and/or MEK inhibitors. A major mode of resistance is reactivation of the MAPK pathway through the upregulation of receptor tyrosine kinase signaling<sup>37,38</sup>, the loss of feedback inhibition<sup>39</sup> and the increase in *NRAS*, *ARAF*, *BRAF*, *CRAF*, *COT* or *MEK1/2* activities in the presence of a MAPK inhibitor (MAPKi)<sup>40–43</sup>. This consistent thread of resistance linked to pathway activation can create cross-resistance among multiple inhibitors. For example, ERK activation can confer resistance to both MEK and BRAF inhibitors. Notably, these mechanisms of resistance leading to increased pathway activation are the very mechanisms that drive the vulnerability of MAPK pathway mutant cells to the knockout of *DUSP4/6*. Therefore, we hypothesized that the development of resistance to MAPKi would hypersensitize cells to the individual and/or dual knockout of *DUSP4/6*. To test this hypothesis, we generated *BRAF* mutant A375 melanoma cells resistant to trametinib and dabrafenib or to trametinib, dabrafenib and SCH772984 and HT144 melanoma cells resistant to dabrafenib only (Fig. 5a and Extended Data Fig. 6a,b).

Resistant cells exhibited markedly increased baseline levels of MAPK signaling (Fig. 5b). To examine the alteration in genetic dependencies between parental and resistant cell lines, we performed genome-wide single-gene CRISPR screens and observed that knockout of *DUSP4* was among the most differential dependencies in both MAPKi-resistant A375 and HT144 cell lines (Fig. 5c–e and Extended Data Fig. 6c). While *DUSP4* was a top hit in the single-gene screens, the dual knockout of *DUSP4/6* had a stronger growth arrest phenotype in MAPKi-resistant cells compared to the knockout of *DUSP4* alone or the parental cells (Fig. 5f). These data strongly suggest that as *BRAF* mutant melanoma cells become resistant to MAPK inhibition, they become simultaneously hypersensitized or ‘cross-sensitized’ to *DUSP4/6* inhibition through the very mechanism that made the cells resistant to the inhibitor.

### Discussion

In this study, we developed an unbiased and systematic approach to identify dependencies of paralogous genes in human cancer cells. Even in the first 11 cell lines screened, we identified both pan-lethal pairs and context-specific synergistic vulnerabilities missed from the single-gene knockout screens. For the latter, we identified *DUSP4/6* as a promising context-dependent lethal combination in *NRAS* and *BRAF* mutant tumors through the hyperactivation of MAPK signaling. This dependency is therefore relevant to 70% of all melanomas. Additionally, the identification of 686 unique digenic dependencies (13.5% of the Digenic Paralog library) across a relatively small number of cell lines raises a question as to what proportion of cancer dependencies consist of functionally redundant gene sets. Expansion of the Digenic Paralog library across additional cell

lines and the examination of genes not included in this study will be required to elucidate a global overview of this space.

Identifying and developing therapeutics for cells resistant to targeted therapies (that is, BRAF and MEK inhibitors) that converge on a common node is challenging<sup>44</sup>. Additionally, identifying a potential dependency where the mechanism of growth arrest is the very mechanism of resistance to small molecule is uncommon (Fig. 5g). Previous studies in vivo have demonstrated that vemurafenib-resistant melanomas show tumor regression on cessation of drug through a similar mechanism described by A375 and HT144 cell lines resistant to MAPKi<sup>41</sup>. Since the mechanism between *DUSP4/6* sensitivity and MAPKi resistance occurs both through hyperactivation of MAPK signaling, this potentially provides an opportunity to reduce the emergence of resistance through intermittent cyclical drug treatment alternating between MAPKi and *DUSP4/6* inhibition. Such a schema would alternately impair viability through pathway downregulation and then pathway upregulation. Due to the cross-sensitizing nature of this paradigm, we hypothesize that RAS pathway-activated melanomas might have few mechanisms of resistant escape to such a treatment schema. In conclusion, functional genomic technologies targeting redundant genes are likely to unveil new druggable targets previously undetected by single-gene knockout approaches.

### Online content

Any methods, additional references, Nature Research reporting summaries, source data, extended data, supplementary information, acknowledgements, peer review information; details of author contributions and competing interests; and statements of data and code availability are available at <https://doi.org/10.1038/s41588-021-00967-z>.

Received: 11 August 2020; Accepted: 14 October 2021;

Published online: 2 December 2021

### References

- McDonald, E. R. 3rd et al. Project DRIVE: a compendium of cancer dependencies and synthetic lethal relationships uncovered by large-scale, deep RNAi screening. *Cell* **170**, 577–592.e10 (2017).
- Behan, F. M. et al. Prioritization of cancer therapeutic targets using CRISPR–Cas9 screens. *Nature* **568**, 511–516 (2019).
- Tsherniak, A. et al. Defining a cancer dependency map. *Cell* **170**, 564–576.e16 (2017).
- Chan, E. M. et al. WRN helicase is a synthetic lethal target in microsatellite unstable cancers. *Nature* **568**, 551–556 (2019).
- Mavrakis, K. J. et al. Disordered methionine metabolism in MTAP/CDKN2A-deleted cancers leads to dependence on PRMT5. *Science* **351**, 1208–1213 (2016).
- Lieb, S. et al. Werner syndrome helicase is a selective vulnerability of microsatellite instability-high tumor cells. *eLife* **8**, e43333 (2019).
- Katagaya, L., Perumal, S. K., Hager, J. H. & Belmont, L. D. Werner syndrome helicase is required for the survival of cancer cells with microsatellite instability. *iScience* **13**, 488–497 (2019).
- Kryukov, G. V. et al. MTAP deletion confers enhanced dependency on the PRMT5 arginine methyltransferase in cancer cells. *Science* **351**, 1214–1218 (2016).
- De Kegel, B. & Ryan, C. J. Paralog buffering contributes to the variable essentiality of genes in cancer cell lines. *PLoS Genet.* **15**, e1008466 (2019).
- Kelly, M. R. et al. Combined proteomic and genetic interaction mapping reveals new RAS effector pathways and susceptibilities. *Cancer Discov.* **10**, 1950–1967 (2020).
- Kuzmin, E. et al. Systematic analysis of complex genetic interactions. *Science* **360**, eaao1729 (2018).
- Tong, A. H. Y. et al. Global mapping of the yeast genetic interaction network. *Science* **303**, 808–813 (2004).
- Costanzo, M. et al. A global genetic interaction network maps a wiring diagram of cellular function. *Science* **353**, aaf1420 (2016).
- Fischer, B. et al. A map of directional genetic interactions in a metazoan cell. *eLife* **4**, e05464 (2015).
- Han, K. et al. Synergistic drug combinations for cancer identified in a CRISPR screen for pairwise genetic interactions. *Nat. Biotechnol.* **35**, 463–474 (2017).

16. Norman, T. M. et al. Exploring genetic interaction manifolds constructed from rich single-cell phenotypes. *Science* **365**, 786–793 (2019).
17. Najm, F. J. et al. Orthologous CRISPR–Cas9 enzymes for combinatorial genetic screens. *Nat. Biotechnol.* **36**, 179–189 (2018).
18. Horlbeck, M. A. et al. Mapping the genetic landscape of human cells. *Cell* **174**, 953–967.e22 (2018).
19. Shen, J. P. et al. Combinatorial CRISPR–Cas9 screens for de novo mapping of genetic interactions. *Nat. Methods* **14**, 573–576 (2017).
20. Zhao, D. et al. Combinatorial CRISPR–Cas9 metabolic screens reveal critical redox control points dependent on the KEAP1–NRF2 regulatory axis. *Mol. Cell* **69**, 699–708.e7 (2018).
21. Hart, T. & Moffat, J. BAGEL: a computational framework for identifying essential genes from pooled library screens. *BMC Bioinformatics* **17**, 164 (2016).
22. Helming, K. C. et al. ARID1B is a specific vulnerability in ARID1A-mutant cancers. *Nat. Med.* **20**, 251–254 (2014).
23. Zamanighomi, M. et al. GEMINI: a variational Bayesian approach to identify genetic interactions from combinatorial CRISPR screens. *Genome Biol.* **20**, 137 (2019).
24. Chen, X. et al. Combined PKC and MEK inhibition in uveal melanoma with GNAQ and GNA11 mutations. *Oncogene* **33**, 4724–4734 (2014).
25. O’Leary, B., Finn, R. S. & Turner, N. C. Treating cancer with selective CDK4/6 inhibitors. *Nat. Rev. Clin. Oncol.* **13**, 417–430 (2016).
26. Park, E. et al. Architecture of autoinhibited and active BRAF–MEK1–14-3-3 complexes. *Nature* **575**, 545–550 (2019).
27. Camps, M., Nichols, A. & Arkininstall, S. Dual specificity phosphatases: a gene family for control of MAP kinase function. *FASEB J.* **14**, 6–16 (2000).
28. Kidger, A. M. & Keyse, S. M. The regulation of oncogenic Ras/ERK signalling by dual-specificity mitogen activated protein kinase phosphatases (MKPs). *Semin. Cell Dev. Biol.* **50**, 125–132 (2016).
29. Unni, A. M., Lockwood, W. W., Zejnullahu, K., Lee-Lin, S.-Q. & Varmus, H. Evidence that synthetic lethality underlies the mutual exclusivity of oncogenic KRAS and EGFR mutations in lung adenocarcinoma. *eLife* **4**, e06907 (2015).
30. Leung, G. P. et al. Hyperactivation of MAPK signaling is deleterious to RAS/RAF-mutant melanoma. *Mol. Cancer Res.* **17**, 199–211 (2019).
31. Brenan, L. et al. Phenotypic characterization of a comprehensive set of MAPK1/ERK2 missense mutants. *Cell Rep.* **17**, 1171–1183 (2016).
32. Goetz, E. M., Ghandi, M., Treacy, D. J., Wagle, N. & Garraway, L. A. ERK mutations confer resistance to mitogen-activated protein kinase pathway inhibitors. *Cancer Res.* **74**, 7079–7089 (2014).
33. Sanchez-Vega, F. et al. Oncogenic signaling pathways in The Cancer Genome Atlas. *Cell* **173**, 321–337.e10 (2018).
34. Unni, A. M. et al. Hyperactivation of ERK by multiple mechanisms is toxic to RTK-RAS mutation-driven lung adenocarcinoma cells. *eLife* **7**, e33718 (2018).
35. Liu, S., Sun, J.-P., Zhou, B. & Zhang, Z.-Y. Structural basis of docking interactions between ERK2 and MAP kinase phosphatase 3. *Proc. Natl Acad. Sci. USA* **103**, 5326–5331 (2006).
36. Peng, D.-J., Zhou, J.-Y. & Wu, G. S. Post-translational regulation of mitogen-activated protein kinase phosphatase-2 (MKP-2) by ERK. *Cell Cycle* **9**, 4650–4655 (2010).
37. Nazarian, R. et al. Melanomas acquire resistance to B-RAF(V600E) inhibition by RTK or N-RAS upregulation. *Nature* **468**, 973–977 (2010).
38. Villanueva, J. et al. Acquired resistance to BRAF inhibitors mediated by a RAF kinase switch in melanoma can be overcome by cotargeting MEK and IGF-1R/PI3K. *Cancer Cell* **18**, 683–695 (2010).
39. Corcoran, R. B. et al. EGFR-mediated re-activation of MAPK signaling contributes to insensitivity of BRAF-mutant colorectal cancers to RAF inhibition with vemurafenib. *Cancer Discov.* **2**, 227–235 (2012).
40. Hatzivassiliou, G. et al. RAF inhibitors prime wild-type RAF to activate the MAPK pathway and enhance growth. *Nature* **464**, 431–435 (2010).
41. Das Thakur, M. et al. Modelling vemurafenib resistance in melanoma reveals a strategy to forestall drug resistance. *Nature* **494**, 251–255 (2013).
42. Johannessen, C. M. et al. COT drives resistance to RAF inhibition through MAP kinase pathway reactivation. *Nature* **468**, 968–972 (2010).
43. Wagle, N. et al. Dissecting therapeutic resistance to RAF inhibition in melanoma by tumor genomic profiling. *J. Clin. Oncol.* **29**, 3085–3096 (2011).
44. Konieczkowski, D. J., Johannessen, C. M. & Garraway, L. A. A convergence-based framework for cancer drug resistance. *Cancer Cell* **33**, 801–815 (2018).

**Publisher’s note** Springer Nature remains neutral with regard to jurisdictional claims in published maps and institutional affiliations.

© The Author(s), under exclusive licence to Springer Nature America, Inc. 2021

## Methods

**Cell lines and reagents.** The MELJUSO (DSMZ), G11 (RIKEN), PK1 (RIKEN), MEWO (ATCC), HS944T (ATCC), IPC298 (DSMZ), A549 (ATCC), HSC5 (JCRB), HS936T (ATCC), PATU8988S (DSMZ), WM2664 (ATCC), MALME3M (ATCC), RVH421 (DSMZ), HS294T (ATCC), A431 (ATCC), A375 (ATCC), PC14 (RIKEN), NCIH1650 (ATCC), NOZ (JCRB), NCIH727 (ATCC) and HT144 (ATCC) cell lines were collected by the Cancer Cell Line Encyclopedia (CCLE). The MEL202 cell line was gifted by M. Jager (Leiden University). All cell lines were grown in medium supplemented with 10% FCS, penicillin ( $100 \mu\text{g ml}^{-1}$ ), streptomycin ( $100 \mu\text{g ml}^{-1}$ ) and L-glutamine ( $292 \mu\text{g ml}^{-1}$ ; Gibco). G11, HS944T, A549, HSS936T, HS294T, PATU8988S and A375 were maintained in DMEM (Gibco). The PK1, MEWO, IPC298, MELJUSO, MEL202, HSC5, WM2664, RVH421, HT144, A431, NCIH1650, NCIH727, PC14 and MALME3M cell lines were maintained in Roswell Park Memorial Institute (RPMI) medium (Gibco). The NOZ cell line was maintained in William's E Medium (Sigma-Aldrich). Culture conditions generated for the Avana dataset are available at <https://depmap.org/>.

**Library production.** The Digenic Paralog CRISPR library was generated using the orthologous *S. pyogenes* and *S. aureus* system. Briefly, oligonucleotide pools were synthesized (Twist Bioscience) with BsmBI sites and appropriate overhang sequences spanning the 20–21 nucleotide (nt) crRNA for *S. pyogenes* and *S. aureus*. Two BbsI sites were designed between the two crRNAs (Supplementary Table 1). Primers were used to amplify the oligonucleotide pools using  $25 \mu\text{l}$  2 $\times$  NEBnext PCR Master Mix (New England Biolabs),  $2 \mu\text{l}$  of oligonucleotide pool (approximately 40 ng),  $5 \mu\text{l}$  of primer mix at a final concentration of  $0.5 \mu\text{M}$  and  $18 \mu\text{l}$  of water. The PCR cycling conditions were: 30 s at  $98^\circ\text{C}$ , 30 s at  $53^\circ\text{C}$ , 30 s at  $72^\circ\text{C}$  for 24 cycles. To clone the pooled crRNA sequences, double-stranded DNA (dsDNA) was purified by spin column (QIAGEN), digested with Esp3I (Thermo Fisher Scientific) and ligated into the Esp3I-digested pRDA\_026 vector using 100 cycles of Golden Gate assembly with a 100-ng insert and 500-ng vector using Esp3I and T7 ligase. pRDA026 is a lentiviral vector with U6 and H1 promoters expressing the two sgRNAs and a short EF1a promoter expressing the SaCas9-2A-puromycin adapted from pPapi (also known as pXPR\_207; plasmid no. 96921; Addgene) by introducing silent mutations at all BbsI sites. To incorporate the tracrRNAs, the purified BbsI-digested *S. pyogenes* and *S. aureus* tracrRNA fragment was cloned in between the dual crRNAs by the second round of Golden Gate assembly (Supplementary Table 1). The ligation product was isopropanol-precipitated and electroporated into Stbl4 electrocompetent cells (Thermo Fisher Scientific) and grown at  $30^\circ\text{C}$  for 16 h on agar with  $100 \mu\text{g ml}^{-1}$  carbenicillin. Colonies were scraped and pDNA was prepared (HiSpeed Plasmid Maxi; QIAGEN).

**Virus production.** Lentivirus production was performed using HEK293T cells as described previously (<https://portals.broadinstitute.org/gpp/public/>). HEK293T were transfected using Lipofectamine 2000 (Thermo Fisher Scientific; for the validation experiments) or LT-1 transfection reagent (Mirus; for the Digenic Paralog library) in T-175 flasks; viral supernatants were filtered before lentiviral infection.

**Paralog library screening.** Cas9 stable cell lines were transduced with a blasticidin-resistant pLX\_311-Cas9 vector (plasmid no. 96924, Addgene; EF1a promoter expressing SpCas9). Before the screening, Cas9-expressing cell lines were selected with blasticidin then transduced with the Digenic Paralog CRISPR library virus in three biological replicates to achieve a representation of 750–1,000 cells per sgRNA and at low multiplicity of infection (MOI; 0.3–0.5; approximately  $2.7 \times 10^6$  cells per replicate). PATU8988S was performed in two biological replicates. Briefly, cell lines were transduced in 12-well plates at  $3.0 \times 10^6$  cells per well in the presence of polybrene with appropriate volume of virus. Plates were centrifuged at 2,000 r.p.m. for 2 h then transferred to a  $37^\circ\text{C}$  incubator for 18 h. Cells were split and treated with puromycin for 3 d. Throughout the screen, cells were split and replated to maintain representation. Cell counts were taken at each passage to monitor growth. Cells were pelleted by centrifugation, resuspended in PBS and processed for gDNA isolation using the NucleoSpin Blood XL (Takara Bio) according to the manufacturer's instructions.

**Sensitizer screen.** Cas9-expressing MELJUSO cells were transduced with the Digenic Paralog library in the presence of DMSO or 78 nM of SCH72984. Briefly, cells were infected as before at an MOI of 0.4 and 1,000 cells per sgRNA. On 3 d of puromycin selection ( $1.5 \mu\text{g ml}^{-1}$ ), cells were then split into three replicates—one replicate in DMSO and two replicates in 78 nM of SCH72984. Cells were passaged continuously in media containing the drug every 3–4 d and collected 15 d after initiation of SCH72984 treatment.

**sgRNA PCR for Illumina sequencing.** The PCR of gDNA and pDNA was performed in multiple 100- $\mu\text{l}$  reactions (total volume) containing a maximum of 10  $\mu\text{g}$  of gDNA or 1 ng of pDNA. DNA was PCR-amplified and barcoded with P5/P7 primers (Integrated DNA Technologies; Supplementary Table 2) using Titanium Taq DNA polymerase (Takara Bio) according to the manufacturer's instructions. Briefly, per one reaction, a PCR master mix consisted of  $2 \mu\text{l}$  of  $50\times$  Titanium Taq polymerase, 10  $\mu\text{l}$  of  $10\times$  Titanium Taq reaction buffer, 8  $\mu\text{l}$  of deoxynucleoside

triphosphate, 0.5  $\mu\text{l}$  of P5 stagger primer mix (stock at  $100\text{-}\mu\text{M}$  concentration) and 19.5  $\mu\text{l}$  of water. Each well consisted of 50  $\mu\text{l}$  of gDNA or pDNA plus water, 40  $\mu\text{l}$  of PCR master mix and 10  $\mu\text{l}$  of a uniquely barcoded P7 primer (stock at  $5\text{-}\mu\text{M}$  concentration). PCR cycling conditions were: an initial 5 min at  $95^\circ\text{C}$  followed by 30 s at  $95^\circ\text{C}$ , 30 s at  $55^\circ\text{C}$ , 20 s at  $72^\circ\text{C}$  for 22 cycles and a final 10-min extension at  $72^\circ\text{C}$ . Samples were purified with Agencourt AMPure XP SPRI beads according to the manufacturer's instructions (catalog no. A63880; Beckman Coulter). Samples were sequenced on a NextSeq 75 base pair (bp)  $\times 2$  paired-end reads (Illumina). Reads were counted by mapping the 20–21 nt sgRNAs to the reference file of all possible sgRNAs present in the library. The resulting matrix of read counts was used in the GEMINI R (v.1.4.0) package to calculate LFCs.

**Paralog gene set.** Paralog pairs were obtained from ENSEMBL (release 91, December 2017). Genes with identified paralogs that shared at least 30% nucleotide sequence identity in either direction were included in the Digenic Paralog library.

**Positive and negative paralog pair controls.** To construct a common set of positive controls for all cell lines, a list of paralogs was generated for 17,936 query genes<sup>45</sup>. A binary loss-of-function matrix (1,611 cell lines by 22,981 genes) was constructed by logic combination of low copy number or deleterious mutation using the CCLE and DepMap data. Low copy number is defined by the relative copy number ( $\log_2$ ) of at least 2 s.d. for each cell line below the mean of all cell lines for a given gene. Deleterious mutations were predicted by frameshift indel or nonsense single-nucleotide variants in whole-exome or whole-genome sequencing. Differential dependency was tested using the DepMap CRISPR dependency scores (probability of dependency) for 659 cell lines and 13,301 genes, which were included in the CRISPR dataset, loss-of-function feature matrix and had at least one annotated paralog. For each gene target in the CRISPR dataset, we performed a two-class comparison of the dependency scores, grouped according to the gene paralog pairs (binary loss-of-function feature). Significant differences in dependency were assessed by a one-sided Kolmogorov–Smirnov test of the continuous dependency score and a one-sided Fisher's exact test of the dependency score binarized at 0.5. This resulted in two *P* values for each dependency paralog pair, which were adjusted using the Benjamini–Hochberg method<sup>46</sup>. Selected synthetic lethal paralog pairs ( $n=21$  of which 10 were included in the Digenic Paralog CRISPR library) had an FDR  $< 0.05$  for at least one of the two significance tests and a mean percentile of both tests in the top 10%. To construct cell line-specific negative controls, we selected genes that were not expressed in each cell line according to the RNA sequencing (RNA-seq) data ( $(\text{TPM} + 1) < 0.1$ ) from the CCLE and annotated paralog pair with both genes not expressed as a non-synergistic pair.

**Validation of paralog synergy hits.** Paralogs identified to have synthetic lethal relationships in the screens were validated using dual *S. pyogenes* Cas9 sgRNA-mediated gene knockout. To reduce recombination, the U6-driven sgRNAs were synthesized with *S. pyogenes* tracrRNA and the H1-driven sgRNA with an alternative *S. pyogenes* tracrRNA variant (CR3; Supplementary Table 1). sgRNAs used in the validation studies were designed using Rule Set 2 (Supplementary Table 3) (ref. <sup>47</sup>). All sgRNAs were synthesized as dsDNA (Twist Bioscience), digested with BsmBI and ligated into pWRS\_1001 (dual U6 and H1 promoters to express the two SpCas9 sgRNAs; EF1a promoter expressing the puromycin selection cassette); inserts were verified by Sanger sequencing (GENEWIZ). For the experiments conducted in Figs. 3e, 4b and 5f and Extended Data Figs. 4e and 5e, viruses containing two individual sgRNAs targeting *DUSP4*, *DUSP6* or both were pooled. The sgRNA used to generate the isogenic sgDUSP6 or sgCHR2 MELJUSO cell lines (Supplementary Table 3) were cloned into pXPR\_016 (U6 promoter expressing sgRNA; EF1a promoter expressing the hygromycin selection cassette). Cells were subsequently infected with tetracycline-inducible vector (catalog no. SVSHU6T17-L; Cellecta) expressing shRNA targeting *DUSP4* or *lacZ* (Supplementary Table 3).

**Generation of ectopic overexpression vectors.** WT and phosphatase-inactive (*DUSP4*<sup>C280S</sup> or *DUSP6*<sup>C293S</sup>) *DUSP4/6* cDNA expression constructs were cloned into modified pLX305-based lentiviral vector driven by a phosphoglycerate kinase 1 promoter (PGK) promoter with an SV40-hygromycin selection cassette. Both WT and phosphatase-inactive *DUSP4/6* cDNAs were constructed to be sgRNA-resistant by introducing 5–6 silent mutations within the sgRNA recognition sites. *lacZ* cDNA was used as a control for the pLX305 vector. WT and mutant (Q61R) *NRAS* cDNAs were cloned into a modified Gateway-compatible pLVX-TetOne-Puro (Takara Bio) inducible vector system. Mutant and WT *ERK2* cDNA were cloned into pLXI\_TRC403 (plasmid no. 111184; Addgene) tetracycline-inducible overexpression lentiviral vector driven by a Tet-responsive promoter with a human PGK-puromycin selection cassette. All cDNAs were generated synthetically (Twist Bioscience) and cloned into a Gateway-compatible pDONR vector. Doxycycline induction of cDNA expression was performed at  $2 \mu\text{M}$  and added fresh every 2 d.

**Coimmunoprecipitation of mutant *ERK2* overexpression constructs.** MELJUSO cells were transduced with the pLXI\_TRC403 vector expressing V5-tagged

green fluorescent protein (GFP), mutant or WT *ERK2*. Cells were treated with or without 2  $\mu\text{M}$  of doxycycline for 48 h. For immunoprecipitation, cells were incubated in lysis buffer (20 mM of Tris-HCl, 10% glycerol, 100 mM of NaCl, 1 mM of EDTA, 5 mM of NaF, 2 mM of  $\text{Na}_3\text{VO}_4$ , 0.2% Triton X-100) plus Halt Protease and phosphatase inhibitors (Thermo Fisher Scientific) for 1 h at 4°C with continuous agitation. Protein lysates were then centrifuged at 13,000g for 15–30 min at 4°C and the supernatant was then transferred to new collection tubes and quantitated using the Pierce BCA Protein Assay Kit (Thermo Fisher Scientific). For coimmunoprecipitation, 2,000  $\mu\text{g}$  of protein was added to 30  $\mu\text{l}$  of prewashed, packed anti-V5 agarose bead slurry (catalog no. A7345; Sigma-Aldrich) and equilibrated to a final volume of 400  $\mu\text{l}$  by adding lysis buffer. Lysate and V5-tagged beads were incubated for 2 h at 4°C with constant gentle agitation. After incubation, antibody-bound lysates underwent three 5-min washes by gently aspirating unbound lysate using a syringe. Each wash was followed by centrifugation at 900–1000g for 1 min at 4°C. Antibody-bound lysate was then boiled at 95–100°C for 10 min before being fractionated, blocked and imaged as described in the immunoblot methods.

**Proliferation assay.** For the proliferation assays, cells were seeded in 96-well plates into 100  $\mu\text{l}$  of medium after lentiviral transduction and antibiotic selection. Cells were seeded at a density of 1,000–2,000 cells per well. At 6–8 d after seeding, cell viability was assessed using the Cell Titer-Glo luminescent cell viability assay (Promega Corporation) by means of an EnVision Multilabel plate reader (PerkinElmer).

**Immunoblotting.** Whole-cell extracts for immunoblotting were prepared by incubating cells on ice in radioimmunoprecipitation assay lysis buffer (Thermo Fisher Scientific) plus Halt Protease and phosphatase inhibitors (Thermo Fisher Scientific) for 30 min. After sonication (30 s) and centrifugation (>15,000 r.p.m., 30 min, 4°C), protein lysates were quantitated using the Pierce BCA Protein Assay Kit. Lysates were fractionated in 4–12% Bis-Tris gel (Invitrogen) and transferred to an Immobilon-FL polyvinylidene fluoride membrane (Sigma-Aldrich) or iBlot nitrocellulose transfer stack (Thermo Fisher Scientific). The membranes were blocked for 1 h with Odyssey Blocking Buffer (TBS) (catalog no. 927-50003; LI-COR Biosciences). The primary antibodies and the dilutions used were as follows: anti-vinculin (1:2,000; catalog no. V9131; Sigma Aldrich); anti-phospho-pERK1/2 (1:1,000, catalog no. 9101; Cell Signaling Technology); anti-ERK1/2 (1:2,000, catalog no. 4696; Cell Signaling Technology); anti-phospho-FRA1 (1:1,000, catalog no. 5841; Cell Signaling Technology); anti-FRA1 (1:100, catalog no. sc-28310; Santa Cruz Biotechnology); anti-DUSP4 (1:1,000, catalog no. 5149; Cell Signaling Technology); anti-DUSP6 (1:500, catalog no. ab76310; Abcam); anti-MKP3 (DUSP6) (1:500, catalog no. sc-377070; Santa Cruz Biotechnology); anti-MEK1 (1:1,000, catalog no. 2352S; Cell Signaling Technology); anti-phospho-MEK1/2 (1:1,000, catalog no. 9154S; Cell Signaling Technology); anti-NRAS<sup>G61</sup> (1:1,000; catalog no. ab222516; Abcam); anti-NRAS (1:500, catalog no. sc-31; Santa Cruz Biotechnology); anti-V5 (1:1,000, catalog no. V8012; Sigma-Aldrich); and anti-GFP (1:1,000, catalog no. 2555S; Cell Signaling Technology). The secondary antibodies IRDye 800CW Goat anti-Rabbit IgG (LI-COR Biosciences) and IRDye 680RD Goat anti-Mouse IgG (LI-COR Biosciences) were used for immunofluorescence staining. Membrane imaging was performed using a near-infrared western blot detection system (LI-COR Biosciences) according to the manufacturer's recommendations.

**AlphaLISA.** ERK1/2 phosphorylation in live cells was assayed using the AlphaLISA SureFire Ultra Kit (PerkinElmer). MELJUSO cells were infected with sgRNA constitutively targeting the chromosome 2 intergenic site (CHR2) or *DUSP6* in combination with doxycycline-inducible shRNA targeting *lacZ* or *DUSP4*. Cells were seeded into 96-well microplates and treated with or without doxycycline for 4 d. Cells were lysed at 4°C in the lysis buffer provided by the manufacturer and ERK1/2 activity was measured according to the manufacturer's protocol using an EnVision Multilabel plate reader. For each experiment, pERK1/2 values were normalized to MELJUSO cells expressing sgCHR2/sh*lacZ* treated with DMSO.

**Generation of drug-resistant cells.** A375 cells were grown in the presence of 1 nM of trametinib and 10 nM of dabrafenib for 145 d. Cells resistant to trametinib and dabrafenib were then withdrawn from the drug and maintained in DMEM supplemented with 10% FCS, penicillin (100  $\mu\text{g ml}^{-1}$ ), streptomycin (100  $\mu\text{g ml}^{-1}$ ) and L-glutamine (292  $\mu\text{g ml}^{-1}$ ). For the cells resistant to trametinib, dabrafenib and SCH772984, the initial pool of trametinib, dabrafenib and SCH772984 cells was subsequently treated with a single-agent of 250 nM of SCH772984 for 28 d and then withdrawn from the drug into regular media. HT144 cells were grown in the presence of 25 nM of dabrafenib for 21 d, withdrawn from the drug and maintained in RPMI supplemented with 10% FCS, penicillin (100  $\mu\text{g ml}^{-1}$ ), streptomycin (100  $\mu\text{g ml}^{-1}$ ) and L-glutamine (292  $\mu\text{g ml}^{-1}$ ). The genome-wide single-gene CRISPR dataset and conditions for the resistant cell lines are available at <https://depmap.org> with the corresponding DepMap IDs ACH-002001, ACH-002003 and ACH-002458.

**Approximation of uncoupling rate.** To estimate the uncoupling rate, the percentage of next-generation sequencing reads that mapped to sgRNA pairs

targeting gene pairs that were not present in the library design were calculated from pDNA and gDNA (day 21) for each cell line.

**Calculation of LFC, synergy and FDR.** The GEMINI R package was used to calculate raw/inferred LFCs (Supplementary Tables 4–7) and synergy scores/statistics (Supplementary Tables 8–13) with their corresponding FDRs. In brief, GEMINI calculates the LFC of the sgRNA pair abundance between pDNA and 21-d postinfection time points. We refer to the mean of LFCs of guide pairs targeting the same gene pair as the raw LFCs. GEMINI employs the LFCs of sgRNA pairs as input and performs a variational Bayesian method to capture CRISPR screen variations while inferring the true gene-level dependencies for individual genes and gene pairs referred to in the manuscript as inferred LFCs. GEMINI computes the sensitive synergy score by comparing the inferred LFC of each gene pair to the most lethal individual gene within the pair. To calculate the FDR, GEMINI uses a set of nonsynergistic pairs in each cell line, as described in the previous section, and constructs the null distributions by fitting a Gaussian mixture model to synergy scores associated with the gene pairs. The *P* value for each gene pair is calculated as the right-tail probability that the null distribution generates a synergy score greater than the score of that pair; FDRs are subsequently calculated based on the Benjamini–Hochberg procedure. The TRIM family was removed from all analyses due to high sequence similarities between family members, significantly increasing the chances of sgRNA off-targets and consequently false paralog discoveries. The sgRNA pair targeting AAVS1 (sgAAVS1-sgAAVS1) was also removed from the analyses due to unexpected high enrichment as a result of uncoupling effects.

**Statistics and reproducibility.** All CRISPR screens were performed in three biological replicates except for PATU8988S, which was performed in biological duplicates. The SCH729984 anchor screen in the MELJUSO cell line was performed in one biological replicate for the DMSO arm and biological duplicates for the SCH729984 arm. The DMSO arm was compared to the three biological replicates from the parental MELJUSO screens for assessing reproducibility. The proliferation assays by CTG were all performed in three biological replicates. Immunoblots are representative images of three biological replicates for Figs. 3d and 4e; biological duplicates for Fig. 5e and Extended Data Fig. 4e,f; and a single replicate for Fig. 4g. Pearson correlation was used for Fig. 1g, Extended Data Figs. 2b,c and 5a (correlation to *BRAF* knockout). LIMMA (v.3.46.0) was used for differential analysis in Fig. 3a and Extended Data Fig. 4b. The Wilcoxon test was used for Fig. 3f and Extended Data Fig. 1b. Point-biserial correlation was used for Extended Data Fig. 5a (correlation to *BRAF* mutation). Linear regression was used for Fig. 4a and Extended Data Fig. 5b–d. Statistical analyses were performed using R v.4.0.3 except for CTG and the AlphaLISA dataset (Prism v.8.4.3 (GraphPad Software)).

**Reporting Summary.** Further information on research design is available in the Nature Research Reporting Summary linked to this article.

## Data availability

The read counts for all screening data and subsequent analyses are provided as Supplementary Data and are available at the Sequence Read Archive under accession no. [PRJNA745952](https://www.ncbi.nlm.nih.gov/sra/PRJNA745952). Paralog identification was obtained from ENSEMBL release 91. All genomic data from the CCLE are available at <https://portals.broadinstitute.org/ccle/data>. DepMap 20Q1 was used for all analyses except for Fig. 5c,d and Extended Data Fig. 6c where DepMap 21Q2 was used. Source data are provided with this paper.

## Code availability

All custom code used for analysis is available on GitHub ([https://github.com/sellerslab/ParalogV1\\_DUSP46](https://github.com/sellerslab/ParalogV1_DUSP46)).

## References

- Viswanathan, S. R. et al. Genome-scale analysis identifies paralog lethality as a vulnerability of chromosome 1p loss in cancer. *Nat. Genet.* **50**, 937–943 (2018).
- Benjamini, Y. & Hochberg, Y. Controlling the false discovery rate: a practical and powerful approach to multiple testing. *J. R. Stat. Soc. Series B Stat. Methodol.* **57**, 289–300 (1995).
- Doench, J. G. et al. Optimized sgRNA design to maximize activity and minimize off-target effects of CRISPR–Cas9. *Nat. Biotechnol.* **34**, 184–191 (2016).

## Acknowledgements

We thank W. Kaelin (Dana-Farber Cancer Institute), M. Meyerson (Dana-Farber Cancer Institute) and L. Lum (Loxo Oncology) for helpful discussions and the Broad Genomics Platform and Genetic Perturbation Platform for their contribution. This work was supported by grants from Ludwig Cancer Research at Harvard (no. 500506) and Broad/IBM Cancer Resistance Research Project (G.G. and L.P.). T.I. is supported by the

Department of Defense Peer Reviewed Cancer Research Program Horizon Award (no. W81XWH-19-1-0271). J.G.D. is supported by the Next Generation Fund at the Broad Institute of MIT and Harvard.

### Author contributions

T.I. and W.R.S. conceived the studies. J.G.D. designed the strategy for library cloning and generated the pRDA\_026 vector. M.Z., T.I., R.L., A.W., S.J. and J.M.K. performed the bioinformatic and statistical analysis. L.C. analyzed the TCGA expression dataset. J.G.D. and D.E.R. provided management support for library cloning. T.I., S.D., M.J.Y. and D.P. performed the CRISPR screens. C.T.L. performed the structural analyses. C.M.J., M.V.R. and B.R.P. generated the resistant cell lines. G.G., L.P. and F.V. provided management support for the Avana DepMap CRISPR screens on resistant cells. T.I., D.M., D.J.R. and M.J.Y. performed the biological validation and analysis. T.I., R.L. and M.Z. prepared the figures and tables for the main text and extended data. T.I. and W.R.S. wrote the manuscript with critical reading and feedback from the other coauthors.

### Competing interests

During the conduct of this research, W.R.S. was or is a Board or Scientific Advisory Board member and equity holder in Peloton Therapeutics, IDEAYA Biosciences, Civetta Therapeutics, Scorpion Therapeutics and Bluebird and has consulted for Array, Astex,

Dynamo Therapeutics, Ipsen, PearlRiver Bio, Sanofi and Servier and receives research funding from Pfizer Pharmaceuticals, Merck, IDEAYA Biosciences and Deerfield Management. J.G.D. consults for Foghorn Therapeutics, Maze Therapeutics, Merck, Agios and Pfizer; he also consults for and has equity in Tango Therapeutics. D.E.R. receives research funding from Functional Genomics Consortium members AbbVie, Janssen, Merck and Vir. G.G. received research funding from IBM and Pharmacyclis and is a founder, consultant and holds private equity in Scorpion Therapeutics. T.I. is a current employee and equity holder of Scorpion Therapeutics. F.V. receives funding from Novo Ventures. C.M.J. is a current Novartis employee and stockholder. A.W. is a current employee of Boehringer Ingelheim. The other authors declare no competing interests.

### Additional information

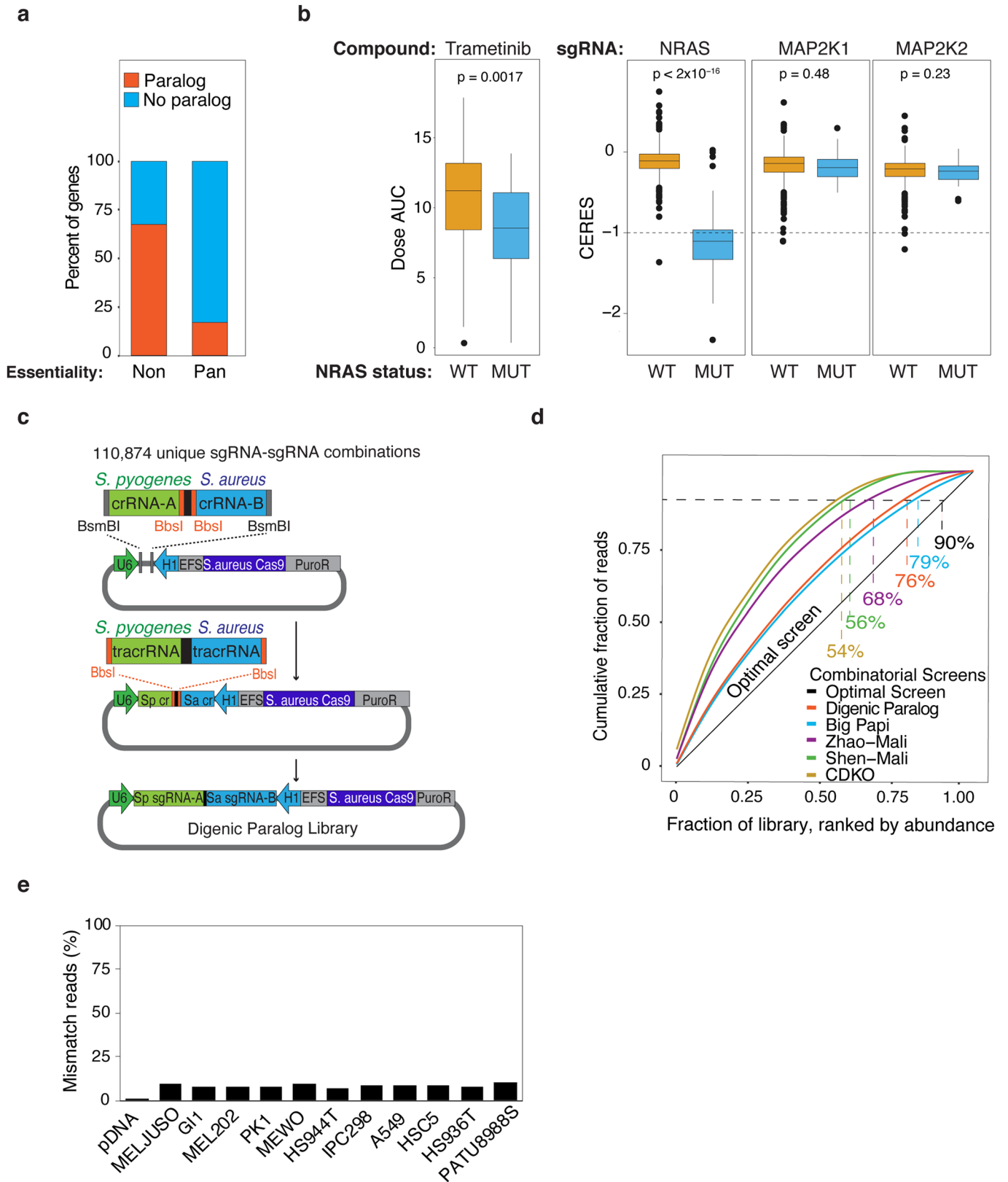
**Extended data** is available for this paper at <https://doi.org/10.1038/s41588-021-00967-z>.

**Supplementary information** The online version contains supplementary material available at <https://doi.org/10.1038/s41588-021-00967-z>.

**Correspondence and requests for materials** should be addressed to William R. Sellers.

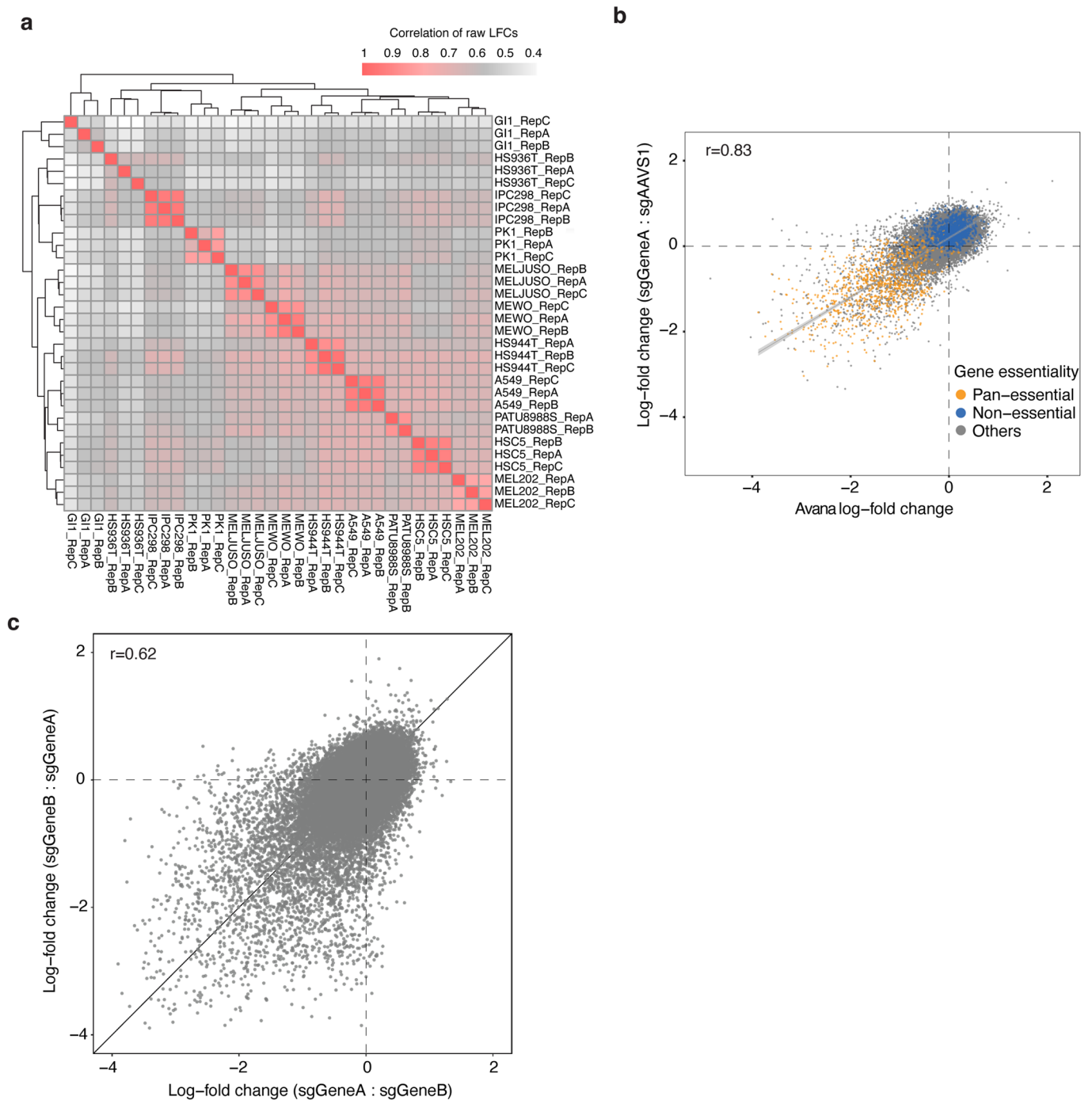
**Peer review information** *Nature Genetics* thanks Peter Jackson and the other, anonymous, reviewer(s) for their contribution to the peer review of this work.

**Reprints and permissions information** is available at [www.nature.com/reprints](http://www.nature.com/reprints).

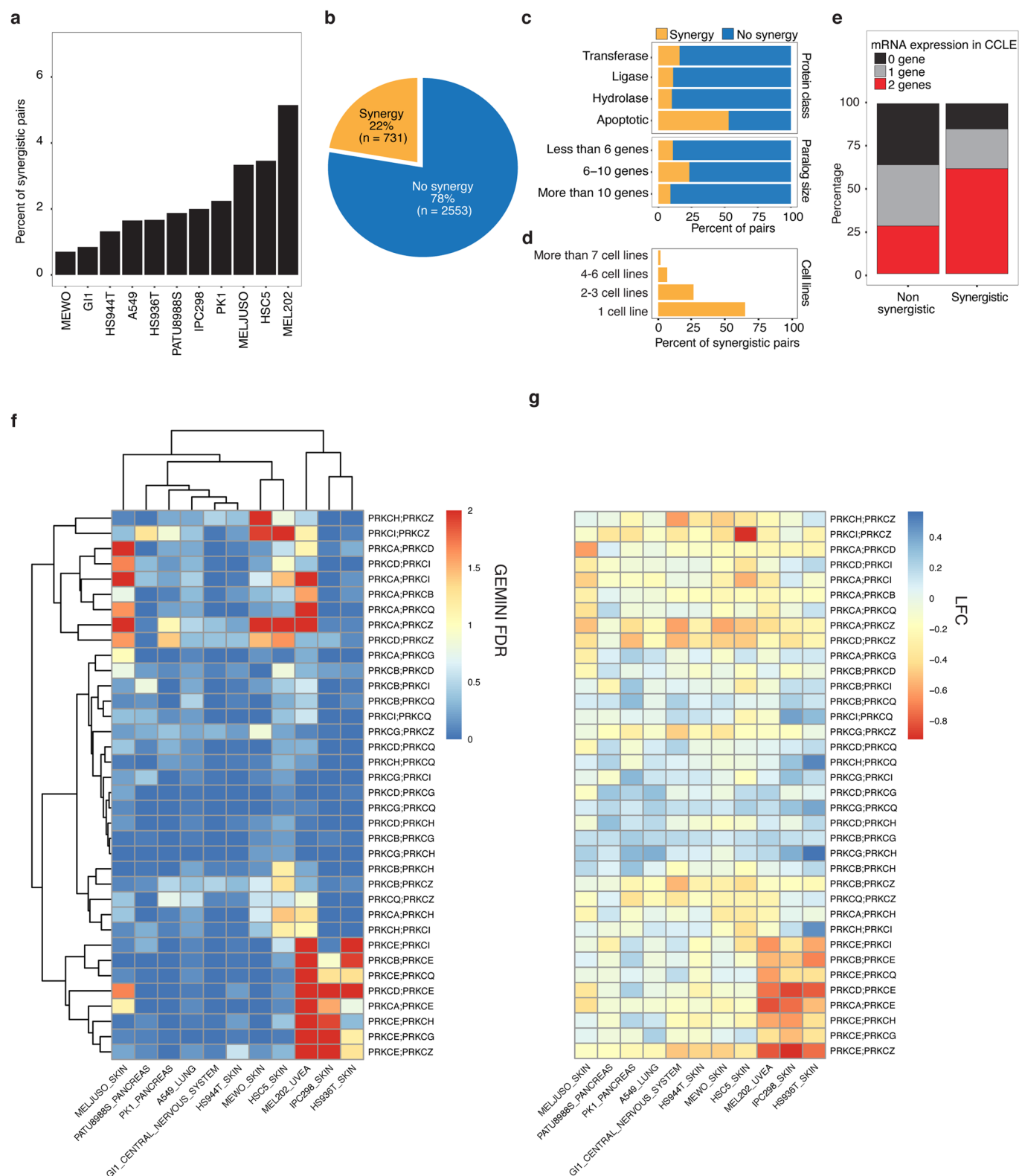


Extended Data Fig. 1 | See next page for caption.

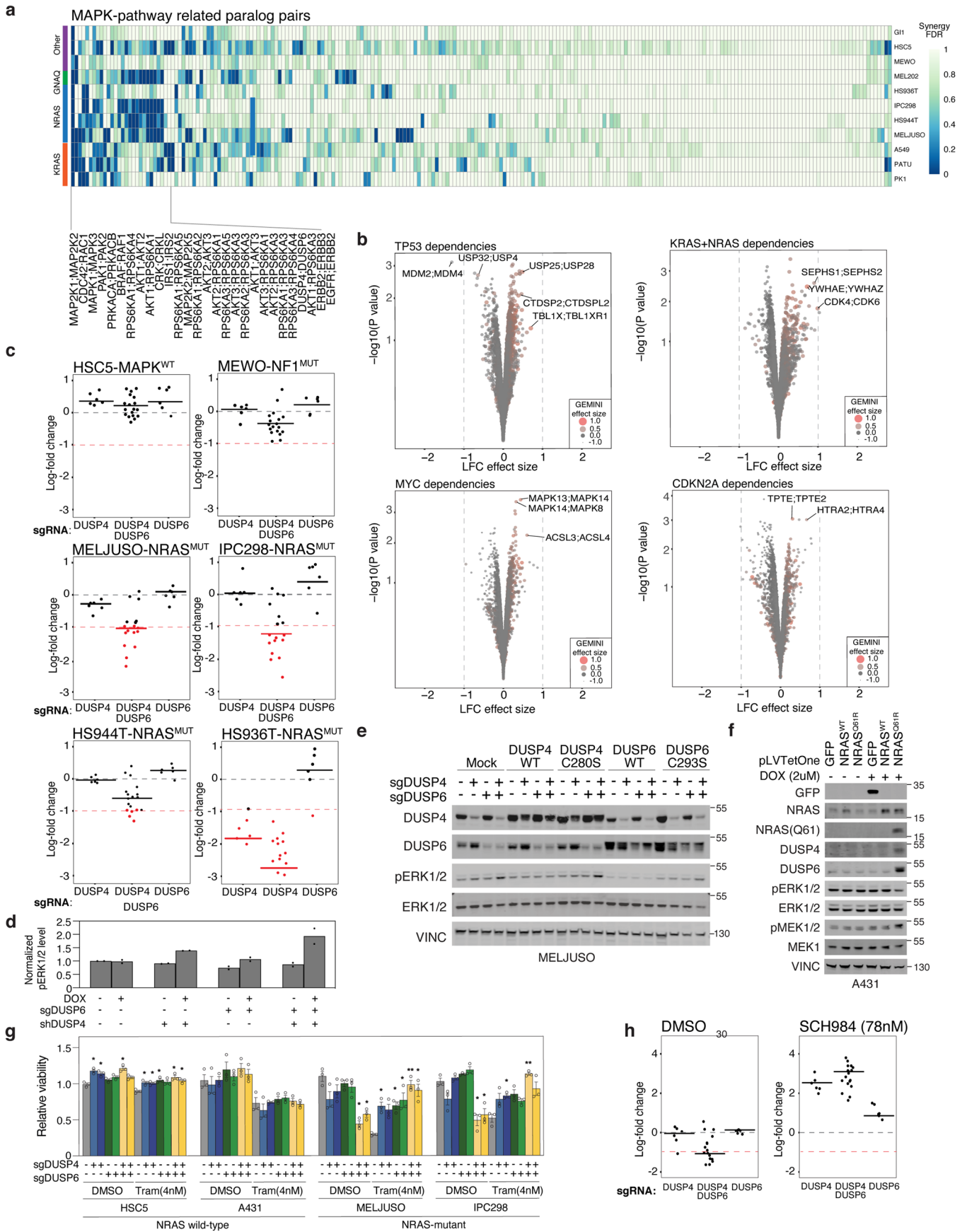
**Extended Data Fig. 1 | Single-gene perturbation screens potentially miss dependencies of functionally paralogous genes.** (a) Stacked bar graph showing the percentage of non-essential or pan-essential human genes with or without paralogs. (b) Box and whisker plots for trametinib (BRD:BRD-K12343256-001-08-9) sensitivity from the Cancer Therapeutics Response Portal (CTRPv2.0\_2015 dataset; <https://portals.broadinstitute.org/ctrp/>). Trametinib was dosed at 16 concentrations in duplicate. Percent-viability curves were fit and the area-under-concentration-response curve (AUC) was calculated. The AUCs of  $NRAS^{MUT}$  (n=31) and  $NRAS^{WT}$  (n=485) cells are shown (*left*).  $NRAS$ ,  $MAP2K1$ , and  $MAP2K2$  CERES dependence scores in  $NRAS^{MUT}$  (n=47) and  $NRAS^{WT}$  (n=692) cells from DepMap screen (*right*). The centerline, lower hinge, and upper hinge correspond to the 50th, 25th, and 75th percentiles, respectively. The upper and lower whiskers extend from the upper and lower hinges to the largest and smallest values no further than  $1.5 * IQR$  (interquartile range). All observations beyond the whiskers are shown in black dots. Two-sided Wilcoxon  $P$ -values are shown. (c) Schematic of the dual sgRNA cloning strategy. (d) Library representation for pDNA from Digenic Paralog, Big Papi, CDKO and early time point gDNA from Shen-Mali (combined from 293T, A549, and HeLa) and Zhao-Mali (combined from A549 and HeLa). (e) Mismatch reads were calculated as the percentage of reads with unintended pairs of sgRNAs from the pDNA and gDNA (at 21 days post library transduction).



**Extended Data Fig. 2 | Robustness and reproducibility of Digenic Paralog CRISPR screens.** (a) Pearson correlation heatmap of raw LFCs between all pairwise combinations of the Digenic Paralog CRISPR screens. (b) Scatterplot of the raw LFC for each gene in the Digenic Paralog CRISPR library against the raw LFC from Avana DepMap CRISPR dataset (20Q1 public dataset) across ten cell lines with available DepMap data. Each dot is annotated by color based on the essentiality profile. Pearson correlation between the two screens was calculated using non-essential and pan-essential genes. (c) Pearson correlation between the average LFC of target guides in position A-B versus position B-A across 11 cell lines.

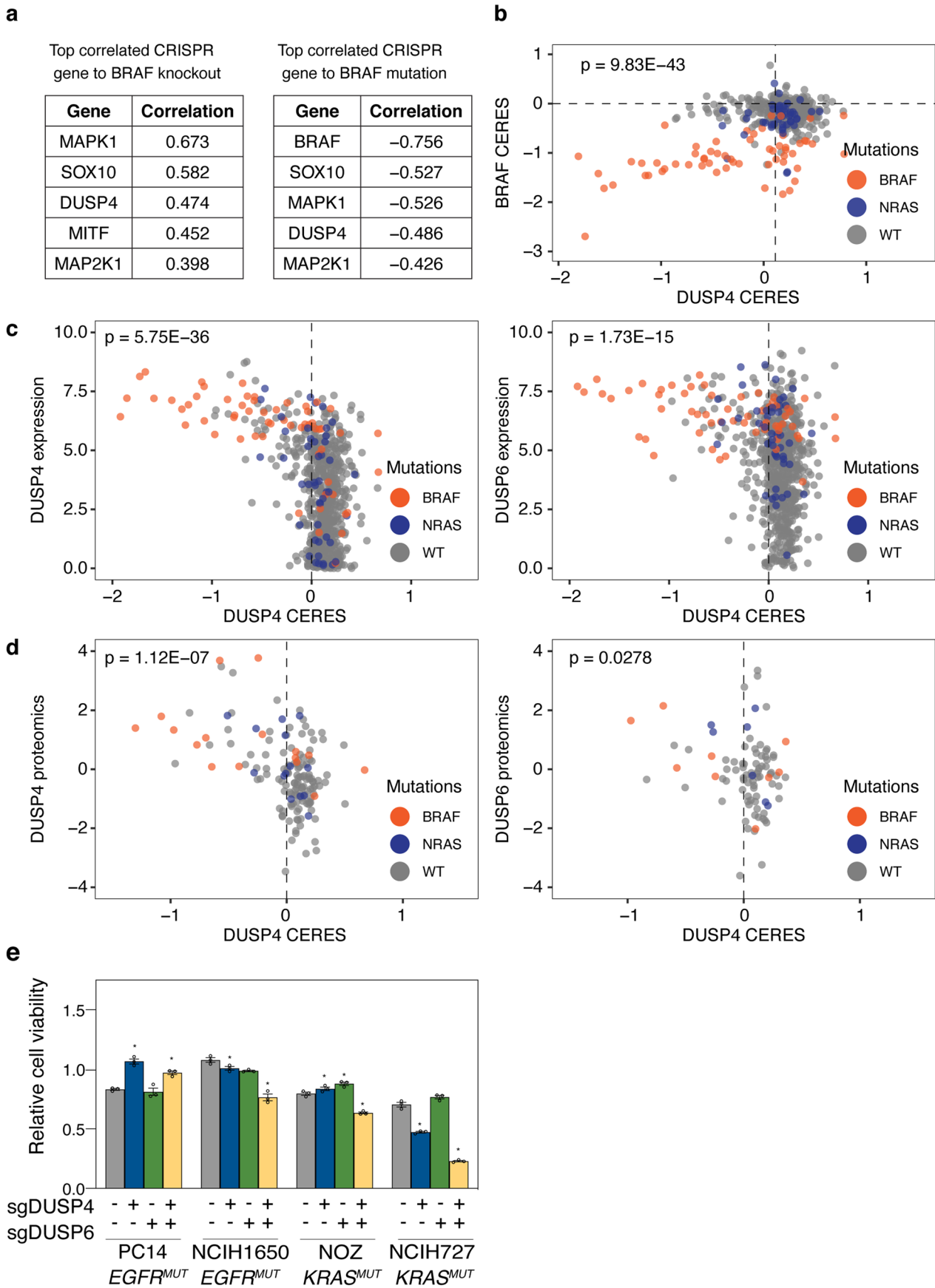


**Extended Data Fig. 3 | Characterization of synergistic paralog genes and selectivity of the PRKC paralog family in GNAQ-mutant uveal melanoma. (a)** Percent of synergistic pairs in the Digenic Paralog CRISPR library with FDR below 5% across 11 cell lines. **(b)** Distribution of genes that exhibited synergy. **(c)** Distribution of paralog pairs that exhibited synergy across protein class (top) and size of paralog family (bottom). **(d)** Frequency of synergistic pairs observed across a varying numbers of cell lines. **(e)** The distribution of non-synergistic pairs and synergistic pairs by whether the genes were expressed across Cancer Cell Line Encyclopedia (CCLE) RNA-seq samples (expressed gene defined as  $\log_2(\text{TPM}+1) > 2$  in at least 50% of 1270 cell lines). **(f)** Heatmap of GEMINI synergy FDRs for gene pairs within the PRKC paralog family. **(g)** Heatmap of the LFC for gene pairs within the PRKC paralog family. Results are shown for individual cell lines.



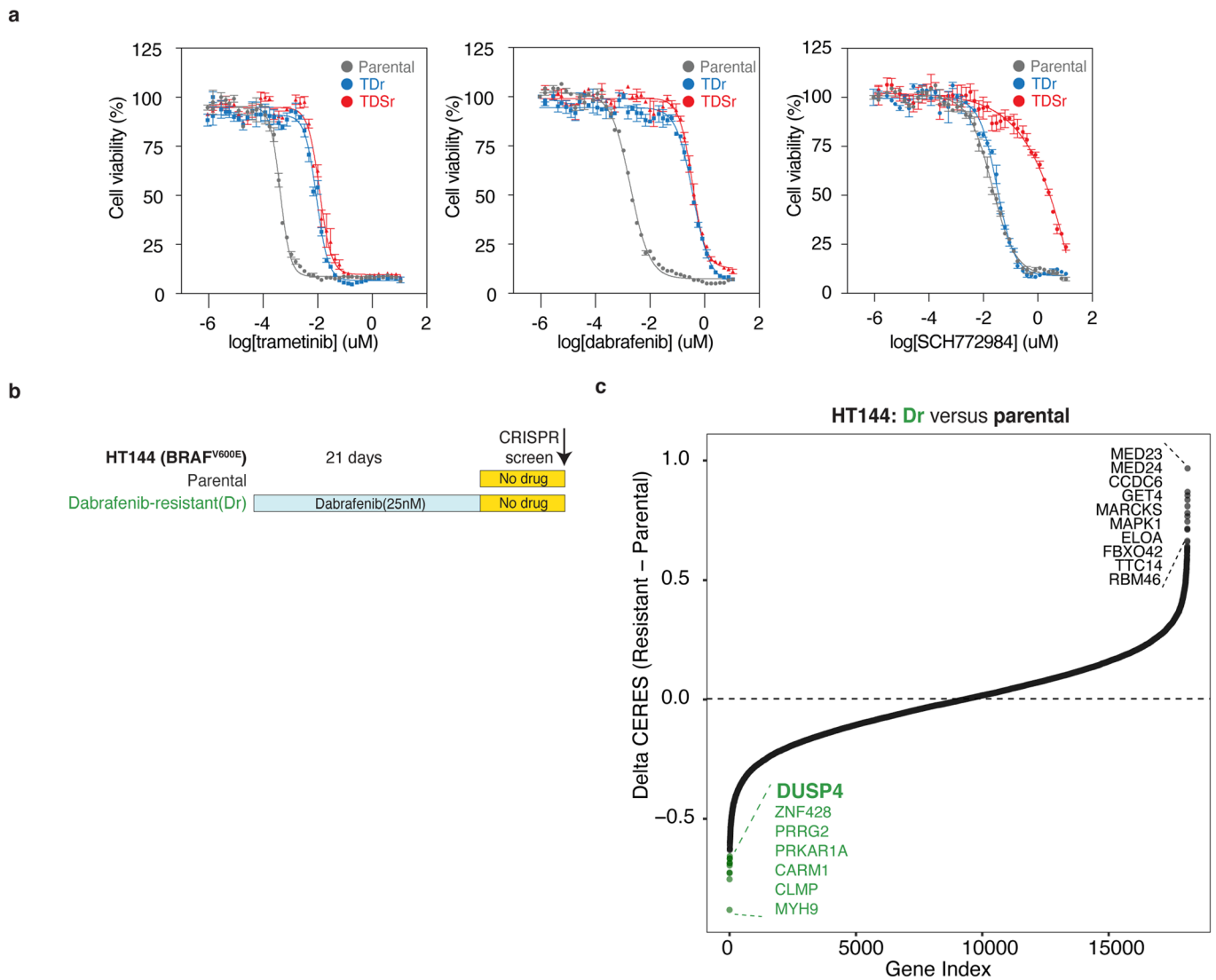
Extended Data Fig. 4 | See next page for caption.

**Extended Data Fig. 4 | DUSP4 and DUSP6 as dependencies in NRAS-mutant cells.** (a) Heatmap of GEMINI synergy FDRs for gene pairs associated with MAPK signaling (KEGG\_MAPK\_SIGNALING\_PATHWAY). (b) Paralog pairs showing differential dependence across indications (*TP53* mutation, *NRAS*/*KRAS* mutation, *MYC* amplification, *CDKN2A* deletion). The mean difference of LFC and P-values (empirical Bayes moderated *t*-test) are plotted. Each point is annotated by the color and size of the mean difference of the GEMINI synergy score. (c) LFCs of individual sgRNAs targeting *DUSP4*, *DUSP6*, or both in indicated cell lines. Inferred LFC is denoted with a line where each dot represents a sgRNA combination. (d) Normalized pERK1/2 (Thr202/Try204) signal. MELJUSO cells were infected with sgRNA targeting chromosome 2 or *DUSP6* in combination with doxycycline (DOX)-inducible shRNA targeting LacZ or *DUSP4*. Cells were treated with or without 2 $\mu$ M of DOX for 4 days and pERK1/2 was measured by AlphaLISA. (e) Immunoblot for *DUSP4*, *DUSP6*, phospho-ERK1/2 and ERK1/2 were performed 2 days following sgRNA transduction and antibiotic selection in MELJUSO cells ectopically expressing sgRNA-resistant wild-type or phosphatase-dead *DUSP4* (C280S) or *DUSP6* (C293S) cDNA and infected with lentivirus producing sgRNAs targeting *DUSP4*, *DUSP6* or both. cDNA expressing LacZ was used as a control. (f) MAPK wild-type squamous cell carcinoma cell line (A431) ectopically expressing DOX-inducible GFP, wild-type *NRAS*, or *NRAS*(Q61R). Cells were treated with 2 $\mu$ M DOX for 2 days and immunoblotted for the indicated proteins. (g) Relative viability in cells infected with a dual promoter lentiviral vector expressing two *S. pyogenes* sgRNAs in presence of DMSO or trametinib (trametinib; 4nM). Two different sgRNAs pairs were used against *DUSP4* or *DUSP6* and sgRNAs targeting AAVS1 and chromosome 2 intergenic sites were used as controls. (h) LFC of individual sgRNAs for *DUSP4*, *DUSP6* or both in DMSO (*left*) or SCH772984 (*right*) treatment. Inferred LFC is denoted with a line where each dot represents a sgRNA combination. The experiment in d was from two independent experiments and g from three independent experiments. Data are mean  $\pm$  s.e.m. \*P-value  $\leq$  0.01, \*\*P-value  $\leq$  0.001, unpaired two-sided *t*-test.



Extended Data Fig. 5 | See next page for caption.

**Extended Data Fig. 5 | Association between DUSP4 dependency and DUSP4/6 levels.** (a) Top 5 genes correlated with *BRAF* CERES score (left - Pearson) or *BRAF* mutation (right - Point-Biserial) from the DepMap screens. (b) Scatterplot of CERES scores for *BRAF* and *DUSP4*. (c) Scatter plot of CERES score for *DUSP4* compared to the expression of *DUSP4* or *DUSP6*. (d) Scatter plot of CERES score for *DUSP4* compared to the mass spectrometry-based proteomics levels of *DUSP4* or *DUSP6*. All expression values are in  $\log_2(\text{TPM} + 1)$ . Proteomic levels are shown as normalized  $\log_2$ -transformed ratios to the bridge sample in each Tandem Mass Tags (TMT) 10-plex. (e) Relative viability of cells infected with sgRNAs pairs targeting *DUSP4* or *DUSP6*. AAVS1 and chromosome 2 intergenic sgRNAs were used as controls. *P*-values were calculated based on linear regression analysis. Experiments in e were from three independent experiments. Data are mean  $\pm$  s.e.m. \**P*-value  $\leq 0.01$ , unpaired two-sided t-test for e. *P*-values for b-d were calculated based on linear regression analysis.



**Extended Data Fig. 6 | Cells resistant to MAPK inhibitors are cross-sensitized to *DUSP4* knockout. (a)** Percent cell viability of parental (gray), TDr (blue), or TDSr (red) A375 cell lines treated with the varying concentrations of trametinib, dabrafenib, or SCH772985 measured after 4 days using CellTiter-Glo. Cell viability was normalized to DMSO control. Data are mean  $\pm$  s.e.m. of biological duplicates. **(b)** Schematic of HT144 cell lines resistant to 25nM dabrafenib (Dr). **(c)** Rank-ordered depiction of the difference in CERES score between HT144 cells resistant to dabrafenib (Dr) and parental HT144 from genome-wide single-gene CRISPR screen. Delta CERES was calculated by CERES HT144<sup>Dr</sup> - CERES HT144<sup>Parental</sup>.

## Reporting Summary

Nature Portfolio wishes to improve the reproducibility of the work that we publish. This form provides structure for consistency and transparency in reporting. For further information on Nature Portfolio policies, see our [Editorial Policies](#) and the [Editorial Policy Checklist](#).

### Statistics

For all statistical analyses, confirm that the following items are present in the figure legend, table legend, main text, or Methods section.

n/a Confirmed

- The exact sample size ( $n$ ) for each experimental group/condition, given as a discrete number and unit of measurement
- A statement on whether measurements were taken from distinct samples or whether the same sample was measured repeatedly
- The statistical test(s) used AND whether they are one- or two-sided  
*Only common tests should be described solely by name; describe more complex techniques in the Methods section.*
- A description of all covariates tested
- A description of any assumptions or corrections, such as tests of normality and adjustment for multiple comparisons
- A full description of the statistical parameters including central tendency (e.g. means) or other basic estimates (e.g. regression coefficient) AND variation (e.g. standard deviation) or associated estimates of uncertainty (e.g. confidence intervals)
- For null hypothesis testing, the test statistic (e.g.  $F$ ,  $t$ ,  $r$ ) with confidence intervals, effect sizes, degrees of freedom and  $P$  value noted  
*Give  $P$  values as exact values whenever suitable.*
- For Bayesian analysis, information on the choice of priors and Markov chain Monte Carlo settings
- For hierarchical and complex designs, identification of the appropriate level for tests and full reporting of outcomes
- Estimates of effect sizes (e.g. Cohen's  $d$ , Pearson's  $r$ ), indicating how they were calculated

*Our web collection on [statistics for biologists](#) contains articles on many of the points above.*

### Software and code

Policy information about [availability of computer code](#)

Data collection

All sequencing were performed using NextSeq 500 (Illumina). Luminescence and absorbance measurements were obtained by the Perkin Elmer EnVision 2105.

Data analysis

Software used: R (V4.0.3), Rstudio (V1.2.5042), GraphPad Prism (V8.4.3), Li-COR Image Studio Lite (V5.2.5), MOE (V2019.0102)

R Packages: import (V1.2.0), grid (V4.0.3), stringi (V1.7.3), stringr (V1.4.0), openxlsx (V4.2.4), mgsub (V1.7.2), ltm (V1.1.1), pbmcapply (V1.5.0), tidyverse (V1.3.1), magrittr (V2.0.1), dplyr (V1.0.7), taigr (V2.8.2.28), ggplot2 (V3.3.5), tidyr (V1.1.3), webr (V0.1.6), gemini (V1.4.0), cellinemapr (V0.1.18), mixtools (V1.2.0), ggrepel (V0.9.1), ggpubr (V0.4.0), ggnewscale (V0.4.5), egg (V0.4.5), limma (V3.46.0), tibble (V3.1.2), plyr (V1.8.6), plotly (V4.9.4.1), readr (V2.0.0), data.table (V1.14.0), purrr (V0.3.4), UpSetR (V1.4.0), ggpmisc (V0.4.0), pheatmap (V1.0.12), scales (V1.1.1), igraph (V1.2.6), RColorBrewer (V1.1.2), nbiomaRt (V2.46.3)

Analysis code are available at: [https://github.com/sellerslab/ParalogV1\\_DUSP46](https://github.com/sellerslab/ParalogV1_DUSP46)

For manuscripts utilizing custom algorithms or software that are central to the research but not yet described in published literature, software must be made available to editors and reviewers. We strongly encourage code deposition in a community repository (e.g. GitHub). See the Nature Portfolio [guidelines for submitting code & software](#) for further information.

## Data

Policy information about [availability of data](#)

All manuscripts must include a [data availability statement](#). This statement should provide the following information, where applicable:

- Accession codes, unique identifiers, or web links for publicly available datasets
- A description of any restrictions on data availability
- For clinical datasets or third party data, please ensure that the statement adheres to our [policy](#)

Analysis code are available at: [https://github.com/sellerslab/ParalogV1\\_DUSP46](https://github.com/sellerslab/ParalogV1_DUSP46)

Database for paralog identification: ENSEMBL (release 91)

NGS sequencing results are available at Sequence Read Archive (SRA): PRJNA745952

Processed LFC and GEMINI scores: Provided in supplementary data

All genomic data from Cancer Cell Line Encyclopedia (CCLE) available at (<https://portals.broadinstitute.org/ccle/data>). DepMap 20Q1 was used for all analyses except for Fig. 5c-d and Extended Data Fig. 6c in which DepMap 21Q2 was used.

## Field-specific reporting

Please select the one below that is the best fit for your research. If you are not sure, read the appropriate sections before making your selection.

- Life sciences       Behavioural & social sciences       Ecological, evolutionary & environmental sciences

For a reference copy of the document with all sections, see [nature.com/documents/nr-reporting-summary-flat.pdf](https://nature.com/documents/nr-reporting-summary-flat.pdf)

## Life sciences study design

All studies must disclose on these points even when the disclosure is negative.

Sample size	<p>Digenic Paralog CRISPR screens in eleven parental cell lines were all performed in biological triplicates of which one replicate was removed from one cell line (PATU8988S - reason shown in Data Exclusion). This is the standard in the field and the high correlation between individual cell lines (Extended Data Fig. 2a) suggests adequate sample size was used.</p> <p>Digenic Paralog CRISPR screens for the drug sensitizer screen in MELJUSO was performed in one biological replicate for the DMSO treated cells as the quality of the screen was assessed against the three biological replicates from the parental MELJUSO cell line screens. MELJUSO cells screened in presence of SCH772984 was performed in biological duplicates.</p> <p>For in vitro validation assays, sample size is indicated in the figure legend for each experiment. The sample size was determined based on previous experience for each experiment to detect specific effects and it was not predetermined with any statistical methods.</p>
Data exclusions	<p>The TRIM family was removed from all bioinformatic analyses due to high sequence similarities between the TRIM family members, significantly increasing chances of sgRNA off-targets. sgRNA pair targeting AAVS1 (sgAAVS1-sgAAVS1) was also removed from the analyses due to unexpected high enrichment as a result of uncoupling effects (describe in Hedge et. al, Plos One 2018).</p> <p>Exclusion criteria for screen was based on correlation between the biological replicate where one replicate out of three from PATU8988S was removed from the all analyses due to the low correlation with the other two biological replicates.</p>
Replication	The replicate correlation of the samples shows the reproducibility (Extended Data Fig. 2a).
Randomization	Samples were not randomized as this question does not pertain to any of the science conducted in this manuscript.
Blinding	Samples were not blinded. Knowledge of the reagents and cell lines were necessary to perform the experiments given different culture condition and transduction efficiencies.

## Reporting for specific materials, systems and methods

We require information from authors about some types of materials, experimental systems and methods used in many studies. Here, indicate whether each material, system or method listed is relevant to your study. If you are not sure if a list item applies to your research, read the appropriate section before selecting a response.

## Materials &amp; experimental systems

## Methods

n/a	Involved in the study
<input type="checkbox"/>	<input checked="" type="checkbox"/> Antibodies
<input type="checkbox"/>	<input checked="" type="checkbox"/> Eukaryotic cell lines
<input checked="" type="checkbox"/>	<input type="checkbox"/> Palaeontology and archaeology
<input checked="" type="checkbox"/>	<input type="checkbox"/> Animals and other organisms
<input checked="" type="checkbox"/>	<input type="checkbox"/> Human research participants
<input checked="" type="checkbox"/>	<input type="checkbox"/> Clinical data
<input checked="" type="checkbox"/>	<input type="checkbox"/> Dual use research of concern

n/a	Involved in the study
<input checked="" type="checkbox"/>	<input type="checkbox"/> ChIP-seq
<input checked="" type="checkbox"/>	<input type="checkbox"/> Flow cytometry
<input checked="" type="checkbox"/>	<input type="checkbox"/> MRI-based neuroimaging

## Antibodies

## Antibodies used

anti-vinculin (Sigma Aldrich, V9131, 1:2000)  
 anti-phospho-pERK1/2 (Cell Signaling Technology, 9101, 1:1000)  
 anti-ERK1/2 (Cell Signaling Technology, 4696, 1:2000)  
 anti-phospho-FRA1 (Cell Signaling Technology, 5841, 1:1000)  
 anti-FRA1 (Santa Cruz Biotechnology, sc-28310, 1:100)  
 anti-DUSP4 (Cell Signaling Technology, 5149, 1:1000)  
 anti-DUSP6 (Abcam, ab76310, 1:500)  
 anti-MKP3 (DUSP6) (Santa Cruz Biotechnology, sc-377070, 1:500)  
 anti-MEK1 (Cell Signaling, 2352S, 1:1000)  
 anti-phospho-MEK1/2 (Cell Signaling, 9154S, 1:1000)  
 anti-NRASQ61 (Abcam, ab222516, 1:1000)  
 anti-NRAS (Santa Cruz Biotechnology, sc-31, 1:500)  
 anti-GFP (Cell Signaling, 2555S, 1:1000)  
 anti-V5 (Sigma, V8012, 1:1000)  
 anti-Rabbit IRDye 800CW (LI-COR, 926-32211, 1:5000)  
 anti-Mouse IRDye 680RD (LI-COR, 926-68070, 1:5000)

## Validation

anti-phospho-pERK1/2 (Cell Signaling Technology, 9101, 1:1000). Antibody detects endogenous levels of p44 and p42 MAP Kinase (Erk1 and Erk2) when phosphorylated either individually or dually at Thr202 and Tyr204 of Erk1 (Thr185 and Tyr187 of Erk2). The antibody does not cross-react with the corresponding phosphorylated residues of either JNK/SAPK or p38 MAP Kinase, and does not cross-react with non-phosphorylated Erk1/2. Reactivity: Human, Mouse, Rat, Hamster, Monkey, Mink, D. melanogaster, Zebrafish, Bovine, Pig, C. elegans. Product citation: Li, L., Puliappadamba, V., Chakraborty, S. et al. EGFR wild type antagonizes EGFRVIII-mediated activation of Met in glioblastoma. *Oncogene* 34, 129–134 (2015). <https://doi.org/10.1038/onc.2013.534>

anti-ERK1/2 (Cell Signaling Technology, 4696, 1:2000). p44/42 MAP Kinase (L34F12) Mouse mAb detects endogenous levels of total p44/42 MAP kinase (Erk1/Erk2) protein. In some systems this antibody may recognize p42/Erk2 more readily than p44/Erk1. The antibody does not cross-react with JNK/SAPK or p38 MAP kinase. Reactivity: Human, Mouse, Rat, Monkey, Mink, Zebrafish, Bovine, Pig. Product citation: Li, L., Puliappadamba, V., Chakraborty, S. et al. EGFR wild type antagonizes EGFRVIII-mediated activation of Met in glioblastoma. *Oncogene* 34, 129–134 (2015). <https://doi.org/10.1038/onc.2013.534>

anti-phospho-FRA1 (Cell Signaling Technology, 5841, 1:1000) Phospho-FRA1 (Ser265) (D22B1) Rabbit mAb recognizes endogenous levels of FRA1 protein only when phosphorylated at Ser265. This antibody may also cross-react with phospho-FRA2, but does not cross-react with phospho-c-Fos or phospho-FosB. Reactivity: Human, Mouse, Rat. Product citation: Vallejo, A., Perurena, N., Guruceaga, E. et al. An integrative approach unveils FOSL1 as an oncogene vulnerability in KRAS-driven lung and pancreatic cancer. *Nat Commun* 8, 14294 (2017). <https://doi.org/10.1038/ncomms14294>

anti-FRA1 (Santa Cruz Biotechnology, sc-28310, 1:100) Fra-1 Antibody (C-12) is a mouse monoclonal IgG1 (kappa light chain) provided at 200 µg/ml raised against amino acids 1-50 of Fra-1 of human origin. Reactivity: mouse, rat, human. Product citation: Iskit S, Schlicker A, Wessels L, Peeper DS. Fra-1 is a key driver of colon cancer metastasis and a Fra-1 classifier predicts disease-free survival. *Oncotarget*. 2015;6(41):43146–43161. doi:10.18632/oncotarget.6454

anti-DUSP4 (Cell Signaling Technology, 5149, 1:1000) DUSP4/MKP2 (D9A5) Rabbit mAb recognizes endogenous levels of total DUSP4 protein. Reactivity: Human and monkey. Product citation: Xue, Z., Vis, D.J., Bruna, A. et al. MAP3K1 and MAP2K4 mutations are associated with sensitivity to MEK inhibitors in multiple cancer models. *Cell Res* 28, 719–729 (2018). <https://doi.org/10.1038/s41422-018-0044-4>.

anti-DUSP6 (Abcam, ab76310, 1:500) Rabbit monoclonal [EPR129Y] to DUSP6. Reactivity: Mouse, rat, human. Product citation: Unni AM, Harbourne B, Oh MH, et al. Hyperactivation of ERK by multiple mechanisms is toxic to RTK-RAS mutation-driven lung adenocarcinoma cells. *Elife*. 2018;7:e33718. Published 2018 Nov 26. doi:10.7554/eLife.33718. Validation: sgRNA against DUSP6.

anti-MKP3 (DUSP6) (Santa Cruz Biotechnology, sc-377070, 1:500) MKP-3 (F-12) is a mouse monoclonal antibody specific for an epitope mapping between amino acids 353-381 at the C-terminus of MKP-3 of human origin. Reactivity: Human, equine, canine, bovine and porcine. Product citation: Unni AM, Harbourne B, Oh MH, et al. Hyperactivation of ERK by multiple mechanisms is toxic to RTK-RAS mutation-driven lung adenocarcinoma cells. *Elife*. 2018;7:e33718. Published 2018 Nov 26. doi:10.7554/eLife.33718. Validation: sgRNA against DUSP6.

anti-MEK1 (Cell Signaling, 2352S, 1:1000) MEK1 (61B2) Mouse mAb detects endogenous levels of total MEK1 protein. This antibody does not cross-react with MEK2 and other MAP kinase kinases. Reactivity: Human, Mouse, Rat, Monkey. Product citation: Hu, W.,

Feng, C. M., et al. (2019), 'TIPE1 Inhibits Breast Cancer Proliferation by Downregulating ERK Phosphorylation and Predicts a Favorable Prognosis.', *Front Oncol*, 9, pp. 400.

anti-phospho-MEK1/2 (Cell Signaling, 9154S, 1:1000) Phospho-MEK1/2 (Ser217/221) (41G9) Rabbit mAb detects endogenous levels of MEK1/2 only when activated by phosphorylation at Ser217/221. Reactivity: Human, Mouse, Rat, Monkey. Product citation: Lu, H., Liu, C., et al. (2020), 'Resistance to allosteric SHP2 inhibition in FGFR-driven cancers through rapid feedback activation of FGFR.', *Oncotarget*, 11 (3), pp. 265-281.

anti-NRASQ61 (Abcam, ab222516, 1:1000) Rabbit monoclonal [EPR20278] to NRAS (mutated Q61). Reactivity: Human. Product citation: N/A

anti-NRAS (Santa Cruz Biotechnology, sc-31, 1:500) N-Ras Antibody (F155) is a high quality monoclonal N-Ras antibody (also designated NRAS antibody) suitable for the detection of the N-Ras protein of mouse, rat and human origin. Reactivity: mouse, rat, human. Product citation: Seibold M, Stühmer T, Kremer N, et al. RAL GTPases mediate multiple myeloma cell survival and are activated independently of oncogenic RAS [published online ahead of print, 2019 Oct 10]. *Haematologica*. 2019;haematol.2019.223024. doi:10.3324/haematol.2019.223024.

anti-GFP (Cell Signaling, 2555S, 1:1000) GFP Antibody detects GFP, YFP, and CFP-tagged proteins exogenously expressed in cells. This antibody does not detect RFP-tagged proteins. Reactivity: all species expected. Product citation: Li, N., Xu, Y., et al. (2019), 'Biallelic ERBB3 loss-of-function variants are associated with a novel multisystem syndrome without congenital contracture.', *Orphanet J Rare Dis*, 14 (1), pp. 265. Validation: sgRNA against GFP.

anti-V5 (Sigma, V8012, 1:1000) Mouse monoclonal V5 antibody specifically detects proteins tagged with V5 (GKPIPPLLGLDST) sequence. We tested the validity of the antibody by tagging GFP with V5 in presence absence of doxycycline expressing the gene. We observed the band corresponding to the correct size only in presence of DOX. This antibody has been validated in over 83 peer-reviewed manuscripts based on [www.citeab.com](http://www.citeab.com).

anti-Rabbit IRDye 800CW (LI-COR, 926-32211, 1:5000) Isolation of specific antibodies was accomplished by affinity chromatography using pooled rabbit IgG covalently linked to agarose. Based on ELISA and flow cytometry, this antibody reacts with the heavy and light chains of rabbit IgG, and with the light chains of rabbit IgM and IgA. Reactivity: rabbit. Product citation: Brenan, L., Andreev, A., Cohen, O., Pantel, S., Kamburov, A., Cacchiarelli, D., Persky, N. S., Zhu, C., Bagul, M., Goetz, E. M., Burgin, A. B., Garraway, L. A., Getz, G., Mikkelsen, T. S., Piccioni, F., Root, D. E., & Johannessen, C. M. (2016). Phenotypic Characterization of a Comprehensive Set of MAPK1/ERK2 Missense Mutants. *Cell reports*, 17(4), 1171–1183. <https://doi.org/10.1016/j.celrep.2016.09.061>.

anti-Mouse IRDye 680RD (LI-COR, 926-68070, 1:5000) Isolation of specific antibodies was accomplished by affinity chromatography using pooled mouse IgG covalently linked to agarose. Based on ELISA and flow cytometry, this antibody reacts with the heavy and light chains of mouse IgG1, IgG2a, IgG2b, and IgG3, and with the light chains of mouse IgM and IgA. Reactivity: Mouse. Product citation: Brenan, L., Andreev, A., Cohen, O., Pantel, S., Kamburov, A., Cacchiarelli, D., Persky, N. S., Zhu, C., Bagul, M., Goetz, E. M., Burgin, A. B., Garraway, L. A., Getz, G., Mikkelsen, T. S., Piccioni, F., Root, D. E., & Johannessen, C. M. (2016). Phenotypic Characterization of a Comprehensive Set of MAPK1/ERK2 Missense Mutants. *Cell reports*, 17(4), 1171–1183. <https://doi.org/10.1016/j.celrep.2016.09.061>.

## Eukaryotic cell lines

Policy information about [cell lines](#)

Cell line source(s)

The MELJUSO (DSMZ), G11 (RIKEN), PK1 (RIKEN), MEWO (ATCC), HS944T (ATCC), IPC298 (DSMZ), A549 (ATCC), HSC5 (JCRB), HS936T (ATCC), PATU8988S (DSMZ), WM2664 (ATCC), MALME3M (ATCC), RVH421(DSMZ), HS294T (ATCC), A431 (ATCC), A375 (ATCC), PC14 (RIKEN), NCIH1650 (ATCC), NOZ (JCRB), NCIH727 (ATCC) and HT144 (ATCC) cell lines were collected by the Cancer Cell Line Encyclopedia (Broad-Novartis) and all Cas9 engineered by expression of pLX311-Cas9 (addgene #1181018) by the Genetic Perturbation Platform (Broad Institute). 293T cell line was obtained from ATCC. The detailed information of the aforementioned cell lines can also be found at [depmap.org](http://depmap.org). MEL202 was gifted by Martine Jager (Leiden University). MEL202 is now commercially available by Millipore-Sigma (Cat#: 13012457-1VL).

Authentication

All cell lines were fingerprinted by SNP arrays and STR profiling.

Mycoplasma contamination

Cell lines were tested negative for mycoplasma.

Commonly misidentified lines  
(See [ICLAC](#) register)

Project Achilles performed fingerprinting to ensure the identify of the screened cell lines. All misidentified cell lines were removed from the final dataset.  
See McDonald, E.R., et al., *Cell*. (2017) for details regarding the cell lines in Project DRIVE.  
Our experiments included no commonly misidentified cell lines as per ICLAC version 9.